Article

Nuclear export of pre-60S particles through the nuclear pore complex

https://doi.org/10.1038/s41586-023-06128-y

Received: 3 October 2022

Accepted: 25 April 2023

Published online: 31 May 2023

Check for updates

Zongqiang Li[1,2,5], Shuaijiabin Chen[1,2,5], Liang Zhao[1,2], Guoqiang Huang[2], Huiqin Xu[1], Xiaoyun Yang[1], Peiyi Wang[3], Ning Gao[4] & Sen-Fang Sui[1,2,3]✉

The nuclear pore complex (NPC) is the bidirectional gate that mediates the exchange of macromolecules or their assemblies between nucleus and cytoplasm[1–3]. The assembly intermediates of the ribosomal subunits, pre-60S and pre-40S particles, are among the largest cargoes of the NPC and the export of these gigantic ribonucleoproteins requires numerous export factors[4,5]. Here we report the cryo-electron microscopy structure of native pre-60S particles trapped in the channel of yeast NPCs. In addition to known assembly factors, multiple factors with export functions are also included in the structure. These factors in general bind to either the flexible regions or subunit interface of the pre-60S particle, and virtually form many anchor sites for NPC binding. Through interactions with phenylalanine-glycine (FG) repeats from various nucleoporins of NPC, these factors collectively facilitate the passage of the pre-60S particle through the central FG repeat network of the NPC. Moreover, in silico analysis of the axial and radial distribution of pre-60S particles within the NPC shows that a single NPC can take up to four pre-60S particles simultaneously, and pre-60S particles are enriched in the inner ring regions close to the wall of the NPC with the solvent-exposed surface facing the centre of the nuclear pore. Our data suggest a translocation model for the export of pre-60S particles through the NPC.

The nuclear pore complex (NPC), embedded in the two-layered nuclear envelope and consisting of more than 500 nucleoporins (Nups), is the largest molecular machine and bidirectional gate mediating the nucleocytoplasmic transport of cellular macromolecules and their assemblies[1–3]. In recent years the intricate three-dimensional (3D) architectures and fine structures of the NPC are now being unveiled through a combination of cryo-electron microscopy (cryo-EM) technology, X-ray crystallography, mass spectrometry and artificial intelligence[6–12].

Ribosome biogenesis is an energy-consuming and orderly regulated process involving more than 200 ribosome assembly factors[4,5]. The assembly of ribosomal subunits starts in the nucleolus, followed by a series of sequential processes including cleavage of ribosomal RNAs and assembly of ribosomal proteins in both nucleolus and nucleoplasm, with the final maturation taking place in the cytoplasm. As one of the bulkiest cargoes to pass through the NPC, the export of preribosomal particles requires multiple, specific nuclear export factors. Many protein factors have been identified as being required for the nuclear export of pre-60S particles, and these need to work in unison to complete the export process[13–20]. In recent years numerous structures of pre-60S ribosomal particles have been reported, covering almost all the major steps of the nuclear and cytoplasmic assembly stages[4,5]. However, these structures contain only very limited structural information for the export process and only three export factors—Bud20, Arx1 and Nmd3—have been visualized in the pre-60S structures of certain nuclear stages[21–23]. This indicates a knowledge gap in the export of the pre-60S particles through the NPC at the molecular level.

Here we employed cryo-EM to analyse endogenous pre-60S ribosomal particles trapped in the channel of NPCs affinity purified from yeast cells, and obtained a unique pre-60S structure at a global resolution at 2.64 Å. A large number of non-ribosomal proteins were identified in this structure, including seven assembly factors and 14 nuclear export factors. The distribution and interaction pattern of these export factors with the phenylalanine-glycine (FG) repeats from the NPC show a general role for these factors in pre-60S export, and suggest a translocation mechanism for the passage of large ribonucleoprotein (RNP) cargoes through the FG repeat-filled pore of the NPC.

Overall structure of NPC-trapped pre-60S

We previously observed that, in yeast NPC particles prepared using tandem-affinity purification[12], an apparent density blob was often located in the NPC central transport channel (Fig. 1a,b). Mass spectrometry results showed that, in addition to known NPC components, many ribosomal proteins and assembly factors were also present in the samples. Freshly prepared NPC samples were then subjected to single-particle cryo-EM analysis, and the images of these unknown density blobs extracted from raw NPC particles were processed with a published map of the pre-60S structure as a reference (EMD-0220)[24]. Classification of particles showed only one predominant population, which was finally

[1]School of Life Sciences, Southern University of Science and Technology, Shenzhen, China. [2]State Key Laboratory of Membrane Biology, Beijing Advanced Innovation Center for Structural Biology, Beijing Frontier Research Center for Biological Structure, School of Life Sciences, Tsinghua University, Beijing, China. [3]Cryo-EM Center, Southern University of Science and Technology, Shenzhen, China. [4]State Key Laboratory of Membrane Biology, Peking-Tsinghua Joint Center for Life Sciences, School of Life Sciences, Peking University, Beijing, China. [5]These authors contributed equally: Zongqiang Li, Shuaijiabin Chen. ✉e-mail: suisf@mail.tsinghua.edu.cn

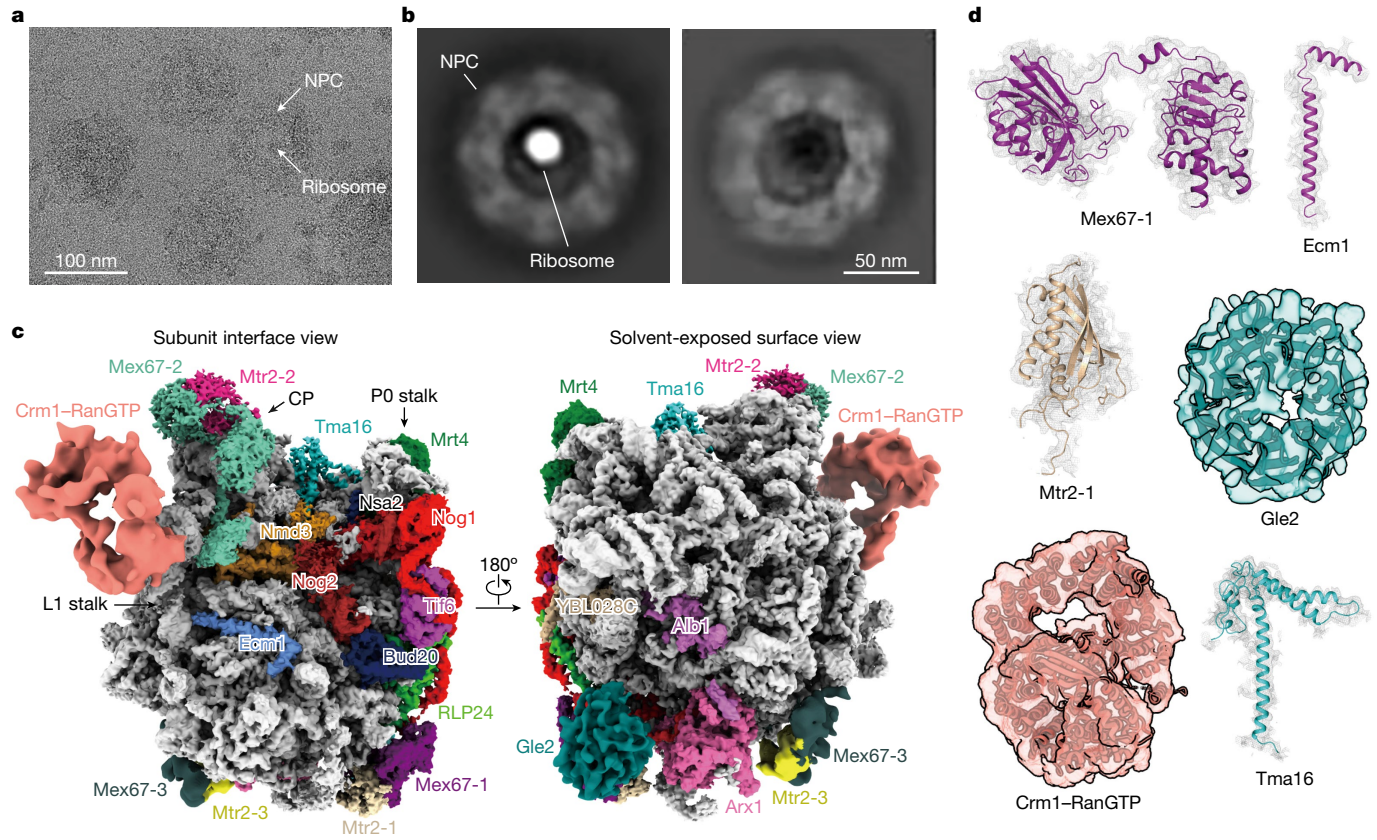

Fig. 1 | Native structure of pre-60S particle trapped in the NPC channel. **a**, Representative raw image of NPC containing a pre-60S particle, from 187,076 similar micrographs. **b**, Representative reference-free, two-dimensional class averages for pre-60S-containing NPC (left) and pre-60S-subtracting NPC (right) from 279,900 particles selected. **c**, Overall structure of NPC-trapped pre-60S particle. Left, subunit interface; right, solvent-exposed surface. Representative assembly factors are colour coded. **d**, Six structurally resolved export factors with their segmented densities.

resolved at a nominal resolution of 2.64 Å (Extended Data Figs. 1 and 2). Starting with a yeast cytoplasmic pre-60S model[25], we built an atomic model for this NPC-trapped pre-60S structure (Extended Data Table 1).

This pre-60S structure is characterized by a unique set of protein components, including 39 ribosomal proteins and 21 non-ribosomal proteins (Fig. 1c and Supplementary Table 1), and is consistent with the current assembly model[4,5], two major structural remodelling events of pre-60S assembly in the nucleus, ITS2 removal and 5S RNP rotation already completed. Different from previous structures of pre-60S particles in the nucleolar, nucleoplasmic and cytoplasmic stages[4,5], 14 factors with nuclear export functions were identified in our structure, ten of which have not been structurally characterized in the context of the pre-60S particle, including three copies of the Mex67–Mtr2 heterodimer (referred to as Mex67–Mtr2-1, -2 and -3), Ecm1, Crm1–RanGTP, Gle2 and Tma16 (Fig. 1c,d). The four remaining factors are Arx1, Alb1, Bud20 and Nmd3. Whereas the first three assemble into the pre-60S particle in the relatively early stages in the nucleolus[21,22,26], Nmd3 incorporates very late in the nucleoplasm[23,27] and is specifically required for recruitment of Crm1 to the pre-60S particle[28,29]. Indeed, using a mask-based local refinement around the region of the C-terminal domain (CTD) of Nmd3, a toroidal density was resolved on the L1 stalk (9.61 Å; Extended Data Fig. 1e) and the atomic model of Crm1–RanGTP (PDB 3NC1) could be roughly fitted in (Fig. 1c,d).

In terms of ribosomal proteins, P1, P2, uL10, uL16, eL24, eL40 and eL41 are clearly missing (Fig. 1c and Supplementary Table 1). Among these, uL10, P1 and P2, together with eL40, are the components of the P0 stalk. The final maturation of the P0 stalk occurs in the cytoplasm and the position of uL10 is currently occupied by a mutually exclusive factor, Mrt4 (refs. 30,31; Fig. 1c). Similarly, the deficiency of uL16, eL24 and eL41 is also consistent with the fact that these proteins are all late binders and assemble in the cytoplasmic stages[23,25]. Overall, the ribosomal protein composition of this NPC-trapped particle is highly consistent with the assembly process of pre-60S particles, indicating that it is a genuine assembly intermediate en route to the cytoplasm.

Structural change in pre-60S through the NPC

This unique structure of NPC-trapped pre-60S particles contains a collection of general nuclear export factors and ribosome-specific nuclear export receptors. This enables structural comparison with known pre-60S structures intermediately before and after nuclear export[25]. One key event before nuclear export is the replacement of Nog2 by Nmd3 (ref. 27). Nog2 is a GTPase proposed to act as a placeholder, and its release enables the subsequent binding of Nmd3 (ref. 27). Previous structures of pre-60S particles indeed showed that both Nmd3 and Nog2 bind to the central region of pre-60S particles and that their core domains are mutually exclusive[22,23,27]. In contrast to this conventional notion, we found that both Nog2 and Nmd3 are present in the structure of the NPC-trapped pre-60S particle. The CTD of Nmd3, well resolved in the map, is in agreement with previous structures[23,25] and is embedded in the transfer RNA corridor of the pre-60S particle (Fig. 2a,b, middle). The N-terminal domain (NTD) of Nmd3, however, is relatively flexible and protrudes into a position occupied by the CTD of Nsa2 in the pre-60S structure of the late nucleocytoplasmic stages (Extended Data Fig. 3a–c)[22]. Consequently, only the NTD of Nsa2 is visible in our structure (Fig. 2a,b, middle). In regard to Nog2, whereas the CTD remains stable—as seen in the pre-60S structure obtained through tandem affinity purification-tagged Nog2 (ref. 22)—its N-terminal

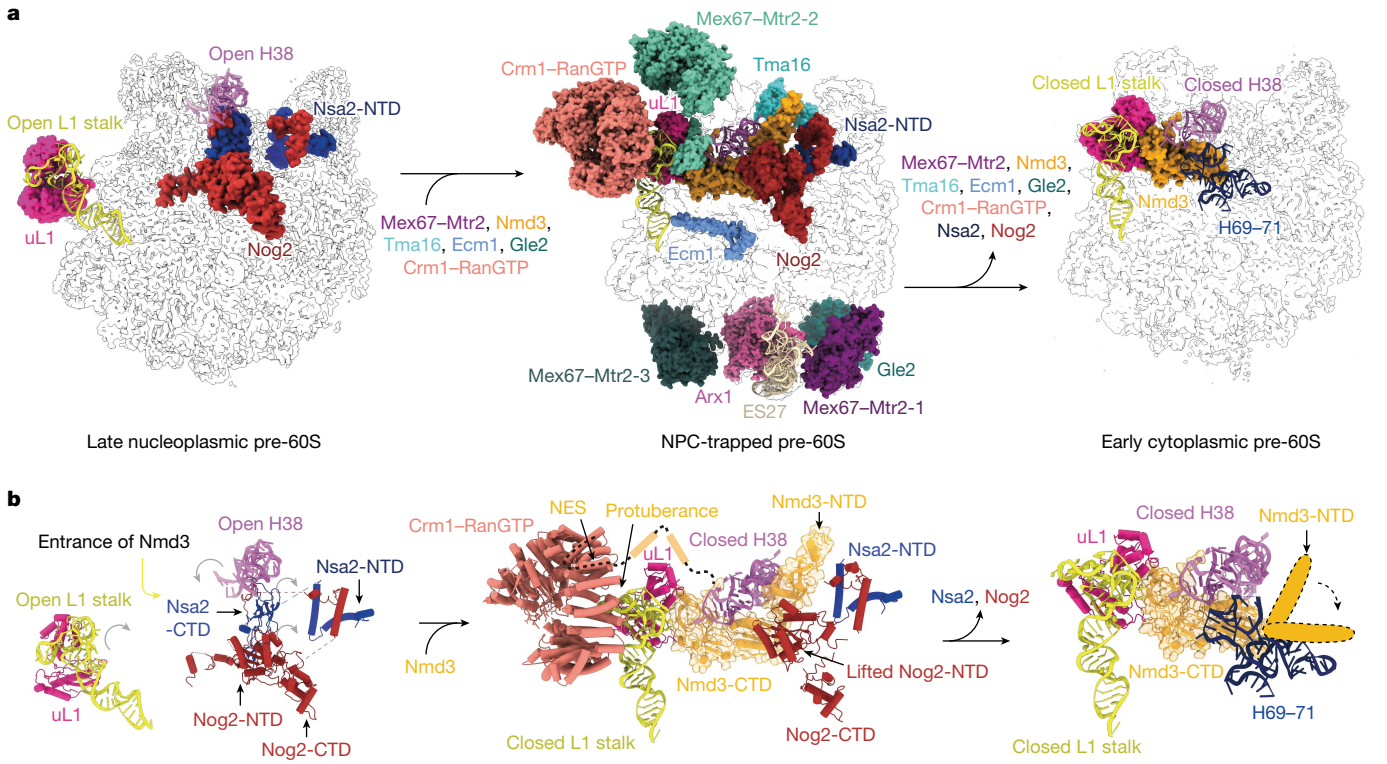

Fig. 2 | Conformational changes in the pre-60S particle following nuclear export. a, Conformational changes of the components of the pre-60S particle before and after nuclear export. On entering the NPC, multiple export factors are assembled into the subunit interface of the pre-60S particle to mask the highly negatively charged protruding rRNA components, and to compact and staple the flexible regions. After nuclear export these export factors, together with Nog2 and Nsa2, are released from the pre-60S particle. The states of pre-60S particles before and after nuclear export are derived from yeast intermediates EMD-0369 and EMD-0370, respectively. **b**, Progressive maturation of the peptidyl transferase centre. Changed components are highlighted in different colours as in **a**. The insertion of Nmd3 induces conformational change of the L1 stalk and H38 from the open to the closed state, resulting in dislodgement of Nog2-NTD and Nsa2-CTD (not resolved in our map) due to steric hindrance by Nmd3-NTD. Subsequent recruitment of Crm1–RanGTP by the C-terminal NES of Nmd3 onto the L1 stalk further stabilizes the closed conformation. After dissociation of Nog2 and Nsa2, the C terminus of Nmd3 moves from the vertical to horizontal state in the cytoplasm (right, orange rod).

GTPase domain appears to be flexible and is dislodged from its position in Nog2 particles (Fig. 2). Another feature of this pre-60S structure is that the central helices, H69–71, are highly flexible, which is consistent with the observation of the structures of Nog2 particles[2] but is in contrast to the cytoplasmic Nmd3-bound pre-60S structures[23,25,32] (Fig. 2). This indicates that the central helices of 25S rRNA in this NPC-trapped particle are undergoing active remodelling (Extended Data Fig. 4). The pre-60S structure intermediately after nuclear export is characterized by a full accommodation of Nmd3 and a near-native conformation of H69–71 (refs. 23,25). Compared with our structure, the NTD of Nmd3 would undergo a large rotation from the NPC-trapped to the early cytoplasmic state (Fig. 2b, right).

An interesting observation is that several known flexible regions of 25S rRNA are surrounded by different sets of proteins (Fig. 3 and Extended Data Fig. 4), including the L1 stalk, H38 and ES27. The L1 stalk adopts an open conformation in Nog2 particles (Fig. 2a,b, left)[22,25,32,33]. Similar to previous structural data[23,25], following the binding of Nmd3 to the NPC-trapped particle the interactions between uL1 and the CTD of Nmd3 induce the L1 stalk into a closed conformation (Fig. 2a,b, middle). H38 also oscillates between open and closed conformation in the late nucleoplasmic assembly stages[22,25]. In our structure H38 is in a tightly packed conformation due to its strong interaction with the C-terminal sequence of Nmd3 (Fig. 2a,b, middle). Unlike previous structures, multiple factors—in addition to Nmd3—contribute to maintaining the closed conformation of the L1 stalk and H38. One Mex67–Mtr2 heterodimer is seen to be sandwiched between the L1 stalk and H38 (Fig. 2a, middle), and the Crm1–RanGTP complex binds to the other side of the L1 stalk opposite uL1. In this way the terminal segments of both H38 and the L1 stalk are encircled by many protein components, including Crm1, uL1, Mex67–Mtr2 and Nmd3 (Fig. 3a,b). In addition, Tma16 and Ecm1 bind to the base region of H38 and the L1 stalk, respectively (Fig. 3a,c). These factors work in unison to sequester the L1 stalk and H38 in a compacted form. The third region is ES27, a known and extremely flexible component near the polypeptide exit tunnel of the pre-60S particle (Extended Data Fig. 4). Compared with the assembly intermediates before and after nuclear export[25], ES27 in the NPC-trapped pre-60S becomes more stable. Arx1, eL38, the N-terminal extension of eL22 and, more importantly, one Mex67–Mtr2 heterodimer around ES27 should collectively contribute to this conformational stabilization (Fig. 3d).

Altogether, our data show that replacement of Nog2 by Nmd3 in the central region of the pre-60S particle is not an instant event but a dynamic process and, most importantly, this process takes place within the NPC. In particular, the NPC-trapped particle is coated with numerous export factors that have sequestered the extruding rRNA helices in compact conformations. Therefore, the decorating and decoating of these export factors before and after nuclear export are expected to be signals triggering certain assembly events.

General export factors for pre-60S particles

Mex67, Mtr2, Crm1 and Gle2 are general export factors, responsible for nuclear export of both mRNAs and preribosomal particles[13,16,34]. Mex67 contains an N-terminal RNA recognition motif (RRM) domain, followed by a leucine-rich repeat (LRR) domain, an NTF2-like domain and a poorly

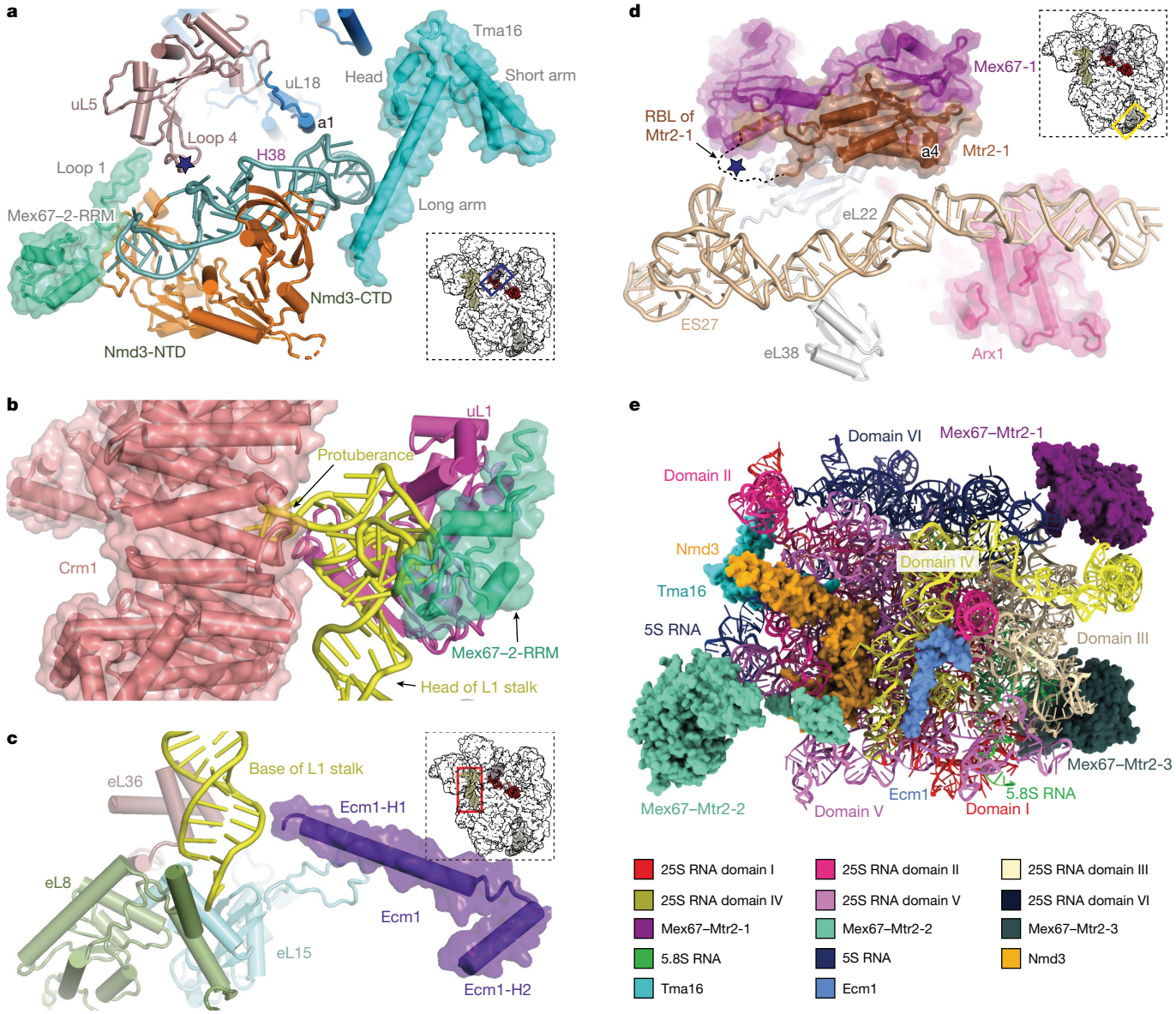

Fig. 3 | Export receptors bind to the flexible regions of the pre-60S particle or to domain junctions of rRNA. a, The RRM domains of Mex67-2, Nmd3, Tma16, uL5 and uL18 embrace H38 in a tightly packed conformation. The positively charged loop from uL5 is indicated by a blue star. The position of H38 (coloured and boxed) in the pre-60S particle is shown in the lower-right thumbnail. **b**,**c**, The closed conformation of the L1 stalk is maintained by Crm1–RanGTP, uL1 and the RRM domain of Mex67-2 in its terminal segment (**b**), and by Ecm1, eL8, eL15 and eL36 in its stem base (**c**). **d**, ES27 is anchored by the loop of Mtr2-1 (blue star), eL22, eL38 and Arx1. **e**, Export factors are distributed around mobile rRNA components and/or in the junctional region of different domains of rRNAs.

conserved ubiquitin-associated domain (Fig. 4a). Mtr2 contains a single NTF2-like domain. Both Mex67 and Mtr2 possess a well-characterized loop in their NTF2-like domain (referred as ribosome-binding loop (RBL) hereafter), which has been demonstrated to be critical for pre-60S binding[13] (Fig. 4a, red star). In the NPC-trapped particle, three Mex67-Mtr2 heterodimers attach to the pre-60S through distinct molecular contacts with relative occupancies Mex67–Mtr2-1 > Mex67–Mtr2-2 > Mex67–Mtr2-3 (Fig. 1c and Extended Data Fig. 9a,b), which may reflect their independent roles in translocation of pre-60S.

Mex67–Mtr2-1 binds to the right side of ES27 (Fig. 2), a position not previously reported. Mex67–Mtr2-1 is the best-resolved dimer among the three (3.8 Å resolution; Extended Data Fig. 1) and it interacts with the pre-60S particle mainly through protein–protein interactions. The RBL of Mex67-1 protrudes into a groove comprising α16 and α17 of Nog1 and α6 of Rlp24 and interacts with two acidic tails from eL31 and eL22 through several positively charged residues. In addition, two positively charged helices—α3 and α5 of the LRR domain—clamp an electronegative loop downstream of Nog1-α18 (Fig. 4b). Both the globular domain of eL22 and H101ES41 of 25S rRNA also contribute to docking of Mex67–Mtr2-1, by interaction with the RBL of Mtr2 and the LRR of Mex67, respectively (Fig. 4c). Importantly, two disease-related mutations (melanoma and uterine cancer) of NXT1, the human homologue of Mtr2, are located next to the RBL of Mtr2-1 (Extended Data Fig. 5a–c and Supplementary Table 2).

Mex67–Mtr2-2 was found in the central protuberance of the pre-60S particle (Fig. 1c). In this position the RBL of Mex67-2, although relatively flexible in the density map, extends towards 5S RNA (Fig. 4d, red star), which is consistent with previous biochemical data showing that the Mex67–Mtr2 heterodimer interacts with 5S RNA[13,35]. Docking of Mex67-2 is facilitated by the interaction between α13 of Mex67-2 and uL18. Similar to the first Mex67–Mtr2 heterodimer, the LRR domain of Mex67-2 also contributes to ribosomal attachment through interactions

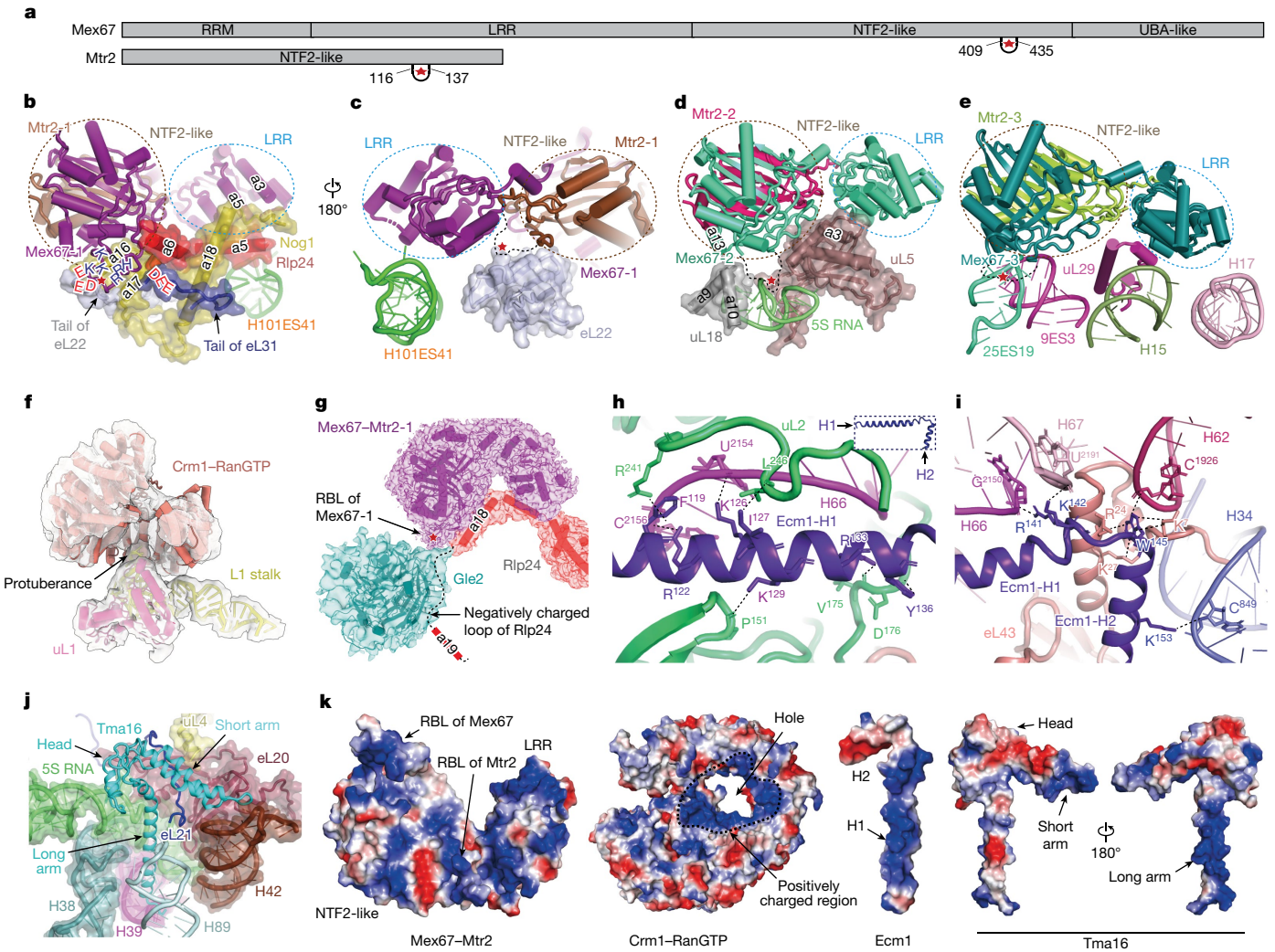

Fig. 4 | Interaction networks between newly identified export factors and the pre-60S particle. a, Schematic representation of the domain organization of Mex67 and Mtr2. RBLs in the NTF2-like domains are indicated by red stars. **b**–**e**, Three Mex67–Mtr2 heterodimers interact with the pre-60S particle. Proteins and rRNAs interacting with Mex67–Mtr2-1 (**b**) and (**c**, horizontally rotated 180° relative to **b**), Mex67–Mtr2-2 (**d**) and Mex67–Mtr2-3 (**e**) are shown and colour coded. NTF2-like and LRR domains are circled by dashed lines. Red stars indicate positions of RBLs from Mex67 and Mtr2. Several charged residues in the RBL of Mex67-1 and surrounding proteins are shown. **f**, The toroidal Crm1–RanGTP is located on top of the L1 stalk through a protuberance (arrow). **g**, Gle2 interacts with Mex67-1 through the RBL (red star and arrow). Based on AlphaFold prediction, the negatively charged loop in the C-terminal tail of Rlp24 (not resolved in our map, arrow) is buried in the basic patch of Gle2. **h**,**i**, Two helices (Ecm1-H1 (**h**) and Ecm1-H2 (**i**) from Ecm1) form extensive electrostatic interactions with H66, uL2, H62, H67, H34 and eL43. **j**, Tma16 stabilizes the central protuberance and the P0 stalk through extensive interactions with 5S RNA, H38, H39, H89, H42, uL4, eL20 and eL21. **k**, Surface electrostatic potentials of Mex67–Mtr2, Crm1–RanGTP, Ecm1 and Tma16 and their interfaces with the pre-60S particle.

with a surface loop of uL5 (Fig. 4d). In this central protuberance-located Mex67–Mtr2 heterodimer, the RRM of Mex67 is stabilized in a region where the L1 stalk, H38, uL1 and the C terminus of Nmd3 meet (Fig. 2a, middle). The extensive interactions between uL1 and the RRM of Mex67 fully explain recent data showing that the failed recruitment of Mex67–Mtr2 caused by *uL1* deficiency leads to delayed export of the large subunit[36]. A conserved Pro58 of NXF1 is located at this L1 stalk interface, and its mutation was found to be associated with severe kidney cancer (Extended Data Fig. 5b and Supplementary Table 2).

Consistent with previous transcriptome-wide cross-linking and analysis of cDNA data[35], the third Mex67–Mtr2 heterodimer is docked on a platform formed by 9ES3 of 5.8S RNA, H15, H17 and 25ES19 of 25S RNA and the N terminus of uL29. In this region, the RBL of Mex67-3 specifically contacts H25ES19 and the LRR mediates the ribosomal interaction with uL29 (Fig. 4e).

Comparisons of three Mex67–Mtr2 heterodimers show that the RBLs of Mex67 and Mtr2, and the LRR of Mex67, are the major components responsible for ribosomal attachment. Whereas the LRR recognizes proteins almost exclusively, the RBLs interact with both proteins and rRNA. Another common feature is that Mex67–Mtr2 interacts with the pre-60S particle mainly through their positive-charge-enriched regions (Fig. 4k). In particular, the binding of Mex67–Mtr2 could potentially mask a large negatively charged surface area of the pre-60S particle, which might be important for the passage of pre-60S particles through the central FG repeat network of the NPC.

Crm1 is a well-studied nuclear exporter factor, functioning in maintaining cellular homeostasis by shuttling a variety of cargoes through the NPC[37] and has been considered an antitumour target[38]. Crm1 in the NPC-trapped particle is located at the top of the L1 stalk (Fig. 4f). Crm1-mediated transportation of cargoes requires a small GTPase Ran[39]. From the density map, an additional density in the centre could be assigned as RanGTP based on the crystal structure of Crm1–RanGTP (PDB 3NC1). It is known that the nuclear export signal (NES) peptide in the C terminus of Nmd3 specifically binds to a hydrophobic

groove between H11 and H12 of Crm1 (Fig. 2b)[40]. Although the C terminus of Nmd3 is relatively flexible in our structure, it is indeed near the NES-binding groove of Crm1 (Fig. 2b). In our structure, docking of Crm1–RanGTP is mediated by direct interactions with the L1 stalk through a positively charged region around the central hole of Crm1 (Fig. 4f,k). Because the L1 stalk is now in a closed position and this conformation is related to the binding of Nmd3 (refs. 23,25,32), this suggests a possible conformation-specific mechanism for the L1 stalk in recruitment of Crm1.

Gle2 is a WD40 domain-containing protein (Extended Data Fig. 6a)[41] that physically interacts with Mex67 (ref. 42) and the NPC[41]. Gle2 was shown to interact specifically with the Gle2-binding sequence of nucleoporins NUP98 (the human orthologue of yeast Nup100) and Nup116 (refs. 16,41,43). Consistent with these data, Gle2 is located next to the Mex67–Mtr2-1 dimer and potentially interacts with the RBL of Mex67-1 (Fig. 4g). Notably, the CTD of Rlp24 is also located near the interface between Mex67 and Gle2 (Fig. 4g). Previous studies have demonstrated that the flexible CTD of Rlp24 is responsible for recruitment of the AAA-ATPase Drg1 to initiate cytoplasmic pre-60S maturation[44], and Drg1 has physical interactions with different nucleoporins including Nup116 (ref. 44). The pre-60S export function of Gle2 could be attributed to a conserved positively charged basic patch on its surface[16] (Extended Data Fig. 6b). Based on the AlphaFold-Multimer-predicted complex structure of Gle2 and Rlp24, this basic patch precisely accommodates a conserved negatively charged motif in the C-terminal tail of Rpl24 (Fig. 4g and Extended Data Fig. 6e,f). Superposition of the NPC-trapped pre-60S particle and the pre-60S–Drg1 complex[45] shows that the Gle2-binding site on pre-60S slightly clashes with the Drg1 hexamer above the entrance of its central channel (Extended Data Fig. 6g). In light of previous studies on the cytoplasmic maturation of the pre-60S particle[46,47] and a recently published study[48], our structure suggests that Gle2 may play a role in guiding the C-terminal tail of Rlp24 into the central channel of the Drg1 hexamer to trigger dissociation of the pre-60S particle from the NPC.

Export receptors in the pre-60S particle

In addition to the above-mentioned general export factors we also identified several nuclear export receptors including Bud20, Arx1, Alb1, Nmd3, Ecm1 and Tma16 (refs. 14,17–19,23,28,32). Among these, Ecm1 and Tma16 have not previously been structurally characterized in the context of yeast pre-60S particles. During model building an extra helical density between the L1 stalk and H34 was identified as Ecm1 (residues 107–159; Extended Data Fig. 3d–g), consistent with recent crosslinking data[49]. In this binding position, whereas helix 1 (H1) of Ecm1 forms extensive interactions with uL2 and H66 of 25S rRNA (Fig. 4h), H2 of Ecm1 lies between H34 and eL43 with relatively fewer contacts. The connecting loop of Ecm1 is situated in a multihelical junction that includes H34, H62, H66 and H67 of 25S rRNA (Fig. 4i).

Similar to human TMA16 (ref. 32), yeast Tma16 exhibits a two-armed structure and binds between the CP and P0 stalk base (Fig. 1c). The long electropositive arm inserts directly into an rRNA-exclusive cavity shaped by 5S RNA, H38, H39 and H89, and the short arm protrudes into the gap between eL20 and H42. The head region anchors to the minor groove of 5S RNA (Fig. 4j,k). Different from the TMA16-containing human pre-60S structures before nuclear export[32], we also identified interactions between Tma16 and ribosomal proteins (uL4, eL20 and eL21; Fig. 4j). Notably, many mutations of conserved residues of Tma16 in the interface have been reported in cancer genomics studies (Extended Data Fig. 5g).

Comparison between the NPC-trapped pre-60S structure with those before and after nuclear export indicates major differences in rRNA in four regions including H38, the L1 stalk, H69–71 and ES27 (Extended Data Fig. 4). Interestingly, all these regions are encircled by export and assembly factors. H38 is surrounded by a collection of factors and ribosomal proteins including Nmd3, the RRM domain of Mex67-2, a positively charged loop of uL5, Tma16 and protuberant helix α1 of uL18 (Fig. 3a). In regard to the L1 stalk, in addition to uL1 this closed conformation is further locked by Crm1 and the RRM domain of Mex67-2 at the top and by Ecm1 at the stem base (Fig. 3b,c). As a highly dynamic rRNA helix, ES27 exhibits a relatively rigid conformation with contributions from the RBL and α4 of Mtr2-1 and Arx1 (Fig. 3d).

In fact, all of the above export factors are either attached to certain mobile rRNA components and/or embedded in the junctional regions of different domains of rRNA (Fig. 3e and Extended Data Fig. 7). Notably, most of these factors bind to the subunit interface (Fig. 5a), which is not fully matured following nuclear export of pre-60S particles. Therefore, this common pattern of export factors in the flexible rRNA regions suggests that they may function in prevention of the prematuration of pre-60S and in reduction of the negative rRNA charge to facilitate nuclear export.

Mechanism of pre-60S nuclear export

Because export factors are located in the outermost shell of the pre-60S particle, they may mediate the interaction of pre-60S particles with the NPC. In addition to Gle2, which can directly interact with the FG-containing nucleoporins NUP98 and Nup116 (refs. 41,43), Mex67 also hosts a FG repeat binding site on the surface of the NTF2-like domain (Fig. 5b,c)[50]. To examine whether this FG-binding property is a shared feature of other export factors in pre-60S particles, we performed local structural refinement with a soft sphere mask centred at each export factor (Methods). As expected, for each export factor a density blob could be found in the refined density map, appearing to be connected to the export factor though weak but identifiable densities (Fig. 5a,b and Extended Data Fig. 8). This observation suggests that blob density could be derived from the central FG Nups and/or NTFs with/without cargoes (CFNC), which is consistent with the reported hydrophobic FG-binding groove of the Mex67 homologue[50] (Fig. 5b,c). In addition to Gle2, Bud20 and three Mex67–Mtr2 dimers, eL19 and YBL028C—a less-studied factor—also directly connected to CFNC densities, suggesting a potential function in pre-60S export (Extended Data Fig. 8a).

Most of the smeared densities of CFNC are on the subunit interface of pre-60S particles (Fig. 5a and Extended Data Fig. 8a), indicating that pre-60S particles trapped inside the NPC are selectively orientated with the subunit interface facing the NPC wall. To validate this, the coordinates of pre-60S particles were first mapped back to the raw NPC particles and the top- and side-view NPC particles were used to calculate the radial and axial distributions of pre-60S particles, respectively (Fig. 5d–f). The results show that the majority of pre-60S particles are located 10 nm distant from the central axis of the NPC, indicating that pre-60S particles are indeed transported close to the wall of the nuclear pore (Fig. 5e). Measured axial distribution shows that pre-60S particles mainly focus on the inner ring region of the NPC (thickness roughly 25 nm; Fig. 5f), indicating a transport intermediate state of pre-60S captured by the purified NPC. Using the same method we then projected the three Mex67–Mtr2 heterodimers. The measured radial distribution showed that Mex67–Mtr2 is mainly focused approximately 10–15 nm (Fig. 5g and Extended Data Fig. 9c–e) closer to the wall of the NPC than the axis of the pre-60S particle, suggesting the preferred orientation during nuclear export of the pre-60S particle. Furthermore, the pre-60S and three Mex67–Mtr2 modules were remapped back to the same NPC, consistent with the above observation (Extended Data Fig. 9f). Another interesting finding is that the NPC could translocate more than one pre-60S particle simultaneously, and up to four pre-60S particles were also observed to reside in the same NPC (Fig. 5h). Although it is difficult for the purified NPC (with a transport channel of around 43 nm)[12] to accommodate more than two orientation-biased pre-60S particles (of approximate diameter 21 nm; Fig. 5a) on the same plane, viewed from the different contrast of the four pre-60S particles

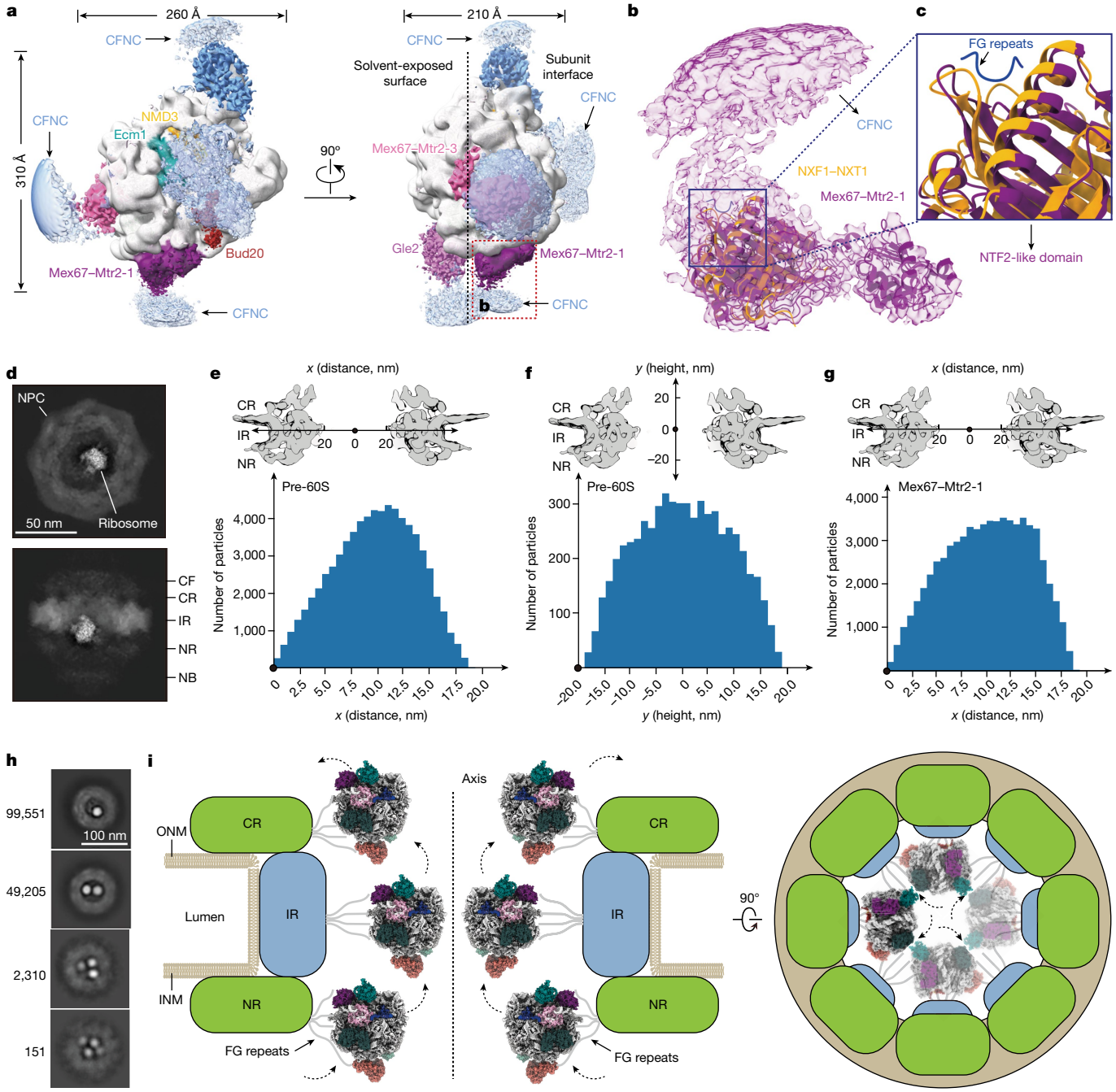

Fig. 5 | Model of the pre-60S particle translocation through the NPC. **a**, Export factors mediate interactions between the pre-60S particle and NPC. Local mask-based refinement of each export factor shows some excess densities, probably from the central FG Nups and/or CFNCs. Mex67–Mtr2-1 is boxed by dotted line and enlarged in **b**. **b**,**c**, Interaction between FG repeats and NTF2-like domain. Models of Mex67–Mtr2 (purple) and NXF1–NXT1 with FG repeats (NXF1–NXT1, orange; FG repeats, blue) (PDB 1JN5) are superposed and fitted to the map of Mex67–Mtr2-1 (**b**), and the region of interaction between FG repeats and the NTF2-like domain (**c**). **d**, Relative position of the pre-60S particle in the NPC in top view (top) and side view (bottom). Images were generated by remapping the coordinates of pre-60S particles back to the relevant entire NPC. **e**,**f**, Radial distribution (**e**) and axial distribution (**f**) of pre-60S particles in the central channel of NPC. **g**, Radial distribution of Mex67–Mtr2-1 in the central channel of NPC. **h**, Typical reference-free, two-dimensional class averages of full NPC particles without subtraction of pre-60S signal. Number of particles in each class is shown on the left. **i**, Model of pre-60S particle translocation through the NPC. CF, cytoplasmic filament; CR, cytoplasmic ring; INM, inner nuclear membrane; IR, inner ring; NB, nuclear basket; NR, nuclear ring; ONM, outer nuclear membrane.

(Fig. 5h) we prefer to think that they are located at different heights along the axis of the NPC. Given the wider inner diameter of native NPC compared with that of purified samples[7], it is possible that more pre-60S particles are transported in parallel under native and/or highly cellular metabolic conditions.

Based on the above observations, we propose a plausible model of pre-60S translocation through the NPC (Fig. 5i). To maximize export efficiency, multiple pre-60S particles can be transported by a single NPC simultaneously. Export-competent pre-60S particles, following binding of export factors, are captured by the central FG repeat network of the NPC on the nucleocytoplasmic side. Because most export factors are located on the hemisphere of the intersubunit face, pre-60S particles are drawn to the NPC wall through interaction with FG repeats emanating from FG Nups, resulting in the solvent-exposed side facing the

centre of the NPC and passing slowly through the nuclear pore from the nuclear ring to the cytoplasmic ring. Given the docking position of Drg1 (ref. 45) on the pre-60S particle and its ability to interact with nucleoporins such as Nup116 (ref. 44), the final release of pre-60S particles from the cytopasmic ring layer of FG repeats may be facilitated by Drg1.

Conclusion

In this work we have characterized the structure of pre-60S particles trapped inside the NPC channel. Structural analysis suggests that nuclear export factors could have two general functions: (1) to prevent prematuration of the pre-60S particle and (2) to bridge interactions between the pre-60S particle and the NPC. These export factors are mainly distributed on the immature subunit interface of pre-60S particles rather than on the mature, solvent-exposed surface, resulting in the transportation of pre-60S particles in a preferred orientation. The predominant distribution of the NPC-trapped pre-60S in inner ring regions might suggest a speed-limiting step and/or a quality control checkpoint. Unexpectedly, multiple pre-60S particles could be transported in parallel in a single nuclear pore to meet the physiological needs of highly active cells. Overall, our work provides a structural framework for understanding the nuclear export of the pre-60S particle through the NPC and shows a translocation mechanism that could also apply to other large RNP cargoes of the NPC. The structure also enables the mapping and analysis of disease-related mutations of various export factors in the context of nuclear export (Extended Data Fig. 5 and Supplementary Table 2).

Online content

Any methods, additional references, Nature Portfolio reporting summaries, source data, extended data, supplementary information, acknowledgements, peer review information; details of author contributions and competing interests; and statements of data and code availability are available at https://doi.org/10.1038/s41586-023-06128-y.

1. Hampoelz, B., Andres-Pons, A., Kastritis, P. & Beck, M. Structure and assembly of the nuclear pore complex. *Annu. Rev. Biophys.* **48**, 515–536 (2019).
2. Lin, D. H. & Hoelz, A. The structure of the nuclear pore complex (an update). *Annu. Rev. Biochem.* **88**, 725–783 (2019).
3. Fernandez-Martinez, J. & Rout, M. P. One ring to rule them all? Structural and functional diversity in the nuclear pore complex. *Trends Biochem. Sci.* **46**, 595–607 (2021).
4. Bassler, J. & Hurt, E. Eukaryotic ribosome assembly. *Annu. Rev. Biochem.* **88**, 281–306 (2019).
5. Klinge, S. & Woolford, J. L. Jr. Ribosome assembly coming into focus. *Nat. Rev. Mol. Cell Biol.* **20**, 116–131 (2019).
6. Kim, S. J. et al. Integrative structure and functional anatomy of a nuclear pore complex. *Nature* **555**, 475–482 (2018).
7. Akey, C. W. et al. Comprehensive structure and functional adaptations of the yeast nuclear pore complex. *Cell* **185**, 361–378 (2022).
8. Zhu, X. et al. Structure of the cytoplasmic ring of the *Xenopus laevis* nuclear pore complex. *Science* **376**, eabl8280 (2022).
9. Mosalaganti, S. et al. AI-based structure prediction empowers integrative structural analysis of human nuclear pores. *Science* **376**, eabm9506 (2022).
10. Bley, C. J. et al. Architecture of the cytoplasmic face of the nuclear pore. *Science* **376**, eabm9129 (2022).
11. Fontana, P. et al. Structure of cytoplasmic ring of nuclear pore complex by integrative cryo-EM and AlphaFold. *Science* **376**, eabm9326 (2022).
12. Li, Z. et al. Near-atomic structure of the inner ring of the *Saccharomyces cerevisiae* nuclear pore complex. *Cell Res.* **32**, 437–450 (2022).
13. Yao, W. et al. Nuclear export of ribosomal 60S subunits by the general mRNA export receptor Mex67-Mtr2. *Mol. Cell* **26**, 51–62 (2007).
14. Yao, Y. et al. Ecm1 is a new pre-ribosomal factor involved in pre-60S particle export. *RNA* **16**, 1007–1017 (2010).
15. Stade, K., Ford, C. S., Guthrie, C. & Weis, K. Exportin 1 (Crm1p) is an essential nuclear export factor. *Cell* **90**, 1041–1050 (1997).
16. Occhipinti, L. et al. Non-FG mediated transport of the large pre-ribosomal subunit through the nuclear pore complex by the mRNA export factor Gle2. *Nucleic Acids Res.* **41**, 8266–8279 (2013).
17. Bassler, J. et al. The conserved Bud20 zinc finger protein is a new component of the ribosomal 60S subunit export machinery. *Mol. Cell. Biol.* **32**, 4898–4912 (2012).
18. Bradatsch, B. et al. Arx1 functions as an unorthodox nuclear export receptor for the 60S preribosomal subunit. *Mol. Cell* **27**, 767–779 (2007).
19. Trotta, C. R., Lund, E., Kahan, L., Johnson, A. W. & Dahlberg, J. E. Coordinated nuclear export of 60S ribosomal subunits and NMD3 in vertebrates. *EMBO J.* **22**, 2841–2851 (2003).
20. West, M., Hedges, J. B., Lo, K. Y. & Johnson, A. W. Novel interaction of the 60S ribosomal subunit export adapter Nmd3 at the nuclear pore complex. *J. Biol. Chem.* **282**, 14028–14037 (2007).
21. Bradatsch, B. et al. Structure of the pre-60S ribosomal subunit with nuclear export factor Arx1 bound at the exit tunnel. *Nat. Struct. Mol. Biol.* **19**, 1234–1241 (2012).
22. Wu, S. et al. Diverse roles of assembly factors revealed by structures of late nuclear pre-60S ribosomes. *Nature* **534**, 133–137 (2016).
23. Ma, C. et al. Structural snapshot of cytoplasmic pre-60S ribosomal particles bound by Nmd3, Lsg1, Tif6 and Reh1. *Nat. Struct. Mol. Biol.* **24**, 214–220 (2017).
24. Thoms, M. et al. Suppressor mutations in Rpf2-Rrs1 or Rpl5 bypass the Cgr1 function for pre-ribosomal 5S RNP-rotation. *Nat. Commun.* **9**, 4094 (2018).
25. Zhou, Y., Musalgaonkar, S., Johnson, A. W. & Taylor, D. W. Tightly-orchestrated rearrangements govern catalytic center assembly of the ribosome. *Nat. Commun.* **10**, 958 (2019).
26. Kater, L. et al. Construction of the central protuberance and L1 stalk during 60S subunit biogenesis. *Mol. Cell* **79**, 615–628 (2020).
27. Matsuo, Y. et al. Coupled GTPase and remodelling ATPase activities form a checkpoint for ribosome export. *Nature* **505**, 112–116 (2014).
28. Gadal, O. et al. Nuclear export of 60s ribosomal subunits depends on Xpo1p and requires a nuclear export sequence-containing factor, Nmd3p, that associates with the large subunit protein Rpl10p. *Mol. Cell. Biol.* **21**, 3405–3415 (2001).
29. Ho, J. H., Kallstrom, G. & Johnson, A. W. Nmd3p is a Crm1p-dependent adapter protein for nuclear export of the large ribosomal subunit. *J. Cell Biol.* **151**, 1057–1066 (2000).
30. Lo, K. Y., Li, Z., Wang, F., Marcotte, E. M. & Johnson, A. W. Ribosome stalk assembly requires the dual-specificity phosphatase Yvh1 for the exchange of Mrt4 with P0. *J. Cell Biol.* **186**, 849–862 (2009).
31. Kemmler, S., Occhipinti, L., Veisu, M. & Panse, V. G. Yvh1 is required for a late maturation step in the 60S biogenesis pathway. *J. Cell Biol.* **186**, 863–880 (2009).
32. Liang, X. et al. Structural snapshots of human pre-60S ribosomal particles before and after nuclear export. *Nat. Commun.* **11**, 3542 (2020).
33. Barrio-Garcia, C. et al. Architecture of the Rix1-Rea1 checkpoint machinery during pre-60S-ribosome remodeling. *Nat. Struct. Mol. Biol.* **23**, 37–44 (2016).
34. Ishizawa, J., Kojima, K., Hail, N. Jr, Tabe, Y. & Andreeff, M. Expression, function, and targeting of the nuclear exporter chromosome region maintenance 1 (CRM1) protein. *Pharmacol. Ther.* **153**, 25–35 (2015).
35. Sarkar, A., Pech, M., Thoms, M., Beckmann, R. & Hurt, E. Ribosome-stalk biogenesis is coupled with recruitment of nuclear-export factor to the nascent 60S subunit. *Nat. Struct. Mol. Biol.* **23**, 1074–1082 (2016).
36. Musalgaonkar, S., Black, J. J. & Johnson, A. W. The L1 stalk is required for efficient export of nascent large ribosomal subunits in yeast. *RNA* **25**, 1549–1560 (2019).
37. Fukuda, M. et al. CRM1 is responsible for intracellular transport mediated by the nuclear export signal. *Nature* **390**, 308–311 (1997).
38. Kosyna, F. K. & Depping, R. Controlling the gatekeeper: therapeutic targeting of nuclear transport. *Cells* **7**, 221 (2018).
39. Monecke, T. et al. Crystal structure of the nuclear export receptor CRM1 in complex with Snurportin1 and RanGTP. *Science* **324**, 1087–1091 (2009).
40. Dickmanns, A., Monecke, T. & Ficner, R. Structural basis of targeting the exportin CRM1 in cancer. *Cells* **4**, 538–568 (2015).
41. Ren, Y., Seo, H. S., Blobel, G. & Hoelz, A. Structural and functional analysis of the interaction between the nucleoporin Nup98 and the mRNA export factor Rae1. *Proc. Natl Acad. Sci. USA* **107**, 10406–10411 (2010).
42. Yoon, J. H., Love, D. C., Guhathakurta, A., Hanover, J. A. & Dhar, R. Mex67p of *Schizosaccharomyces pombe* interacts with Rae1p in mediating mRNA export. *Mol. Cell. Biol.* **20**, 8767–8782 (2000).
43. Bailer, S. M. et al. Nup116p and nup100p are interchangeable through a conserved motif which constitutes a docking site for the mRNA transport factor gle2p. *EMBO J.* **17**, 1107–1119 (1998).
44. Kappel, L. et al. Rlp24 activates the AAA-ATPase Drg1 to initiate cytoplasmic pre-60S maturation. *J. Cell Biol.* **199**, 771–782 (2012).
45. Prattes, M. et al. Visualizing maturation factor extraction from the nascent ribosome by the AAA-ATPase Drg1. *Nat. Struct. Mol. Biol.* **29**, 942–953 (2022).
46. Lo, K. Y. et al. Defining the pathway of cytoplasmic maturation of the 60S ribosomal subunit. *Mol. Cell* **39**, 196–208 (2010).
47. Altvater, M. et al. Targeted proteomics reveals compositional dynamics of 60S pre-ribosomes after nuclear export. *Mol. Syst. Biol.* **8**, 628 (2012).
48. Ma, C., Wu, D., Chen, Q. & Gao, N. Structural dynamics of AAA + ATPase Drg1 and mechanism of benzo-diazaborine inhibition. *Nat. Commun.* **13**, 6765 (2022).
49. Sailer, C. et al. A comprehensive landscape of 60S ribosome biogenesis factors. *Cell Rep.* **38**, 110353 (2022).
50. Fribourg, S., Braun, I. C., Izaurralde, E. & Conti, E. Structural basis for the recognition of a nucleoporin FG repeat by the NTF2-like domain of the TAP/p15 mRNA nuclear export factor. *Mol. Cell* **8**, 645–656 (2001).

Methods

Affinity purification of native *Saccharomyces cerevisiae* NPC

The native *S. cerevisiae* NPC (*sc*NPC) sample was prepared as previously described[12]. Briefly, yeast strain *Mlp1-PrA/Nup84-3FH*, with protein A and 3× FLAG plus 10× His-tags in endogenous *Mlp1* and *Nup84*, respectively, was grown at 30 °C to mid-log phase then treated with 10 μg ml^{-1} alpha-mating factor (α-factor) for 2 h to synchronize cells before harvesting by centrifugation. Treatment of α-factor arrests cells in the G1 phase, in which synthesis occurs of various enzymes and nutrients subsequently required for DNA replication and cell division, increasing the probability of capturing ribosomes through the NPC. The collected yeast cells were quickly frozen in liquid nitrogen followed by cryogenic grinding in a mill. Resuspended lysate was used for affinity purification of endogenous NPC successively through anti-FLAG beads (MERCK, no. A2220), a Sephacryl S-500 HR column (GE Healthcare, HiPrepTM 16/60 Sephacryl S-500 HR) and Dynabeads (Thermo Fisher, no. 14311D) coupled to rabbit IgG antibodies (Sigma-Aldrich, no. I5006, 10 mg). Finally, the eluted sample containing the *sc*NPC was collected and centrifuged at 20,000*g* for 10 mins.

Cryo-EM sample preparation and single-particle dataset acquisition

Cryo-EM samples of *sc*NPC were prepared according to a previous method[12]. In short, purified samples with 10% glycerol were checked by negative staining using a Tecnai Spirit at 120 kV (Thermo Fisher Scientific). Samples with the highest homogeneity were subjected to cryo-EM sample preparation. Next, 200-mesh Au-lacey carbon grids with continuous carbon support film (Electron Microscopy Sciences) were glow discharged in air and each grid was mounted on forceps in a Mark IV Vitrobot (Thermo Fisher Scientific) at 4 °C and 100% humidity. Sample drops (4 μl) were floated on the grid for 60 s and then about 3 μl removed by pipettor absorption. Elution buffer (4 μl) without glycerol was added to the grid and the grid plunge-frozen in liquid ethane after blotting.

Datasets of the NPC complex were collected on a Titan Krios electron microscope operating at 300 kV and equipped with a Gatan K3 Summit direct electron detector and a GIF Quantum energy filter. All datasets were collected using SerialEM[51] with the same imaging settings. Untilted images were recorded using a pixel size of 0.668 Å and magnification of ×130,000. The defocus value was set between −1.5 and −2.5 μm during data collection. Each micrograph was dose fractioned into 32 frames with a total dose of about 50 $e^{-}/Å^{2}$. Tilted 40° images were recorded using a pixel size of 1.356 Å and magnification of ×64,000. The defocus value was set between −1.5 and −2.5 μm during data collection. Each micrograph was dose fractioned into 50 frames with a total dose of about 50 $e^{-}/Å^{2}$.

Finally, 296,820 and 92,427 videos were collected for the untilted and tilted datasets, respectively. The beam-induced motion of the whole micrograph was corrected by MotionCor2 (ref. 52). Contrast transfer function (CTF) parameters were estimated by Patch CTF estimation in cryoSPARC 3.2 (ref. 53) for the NPC.

Image processing

pre-60S reconstruction. The detailed workflow for data-processing procedures is summarized in Extended Data Fig. 1. In general, raw video stacks were motion corrected using MotionCor2 or cryoSPARC 3.2 and the defocus values of each micrograph were estimated using Patch CTF estimation in cryoSPARC, Gctf[54] or CTFFIND4.1 (ref. 55). Particle picking was carried out in cryoSPARC as previously described[12]. A total of 279,900 particles were finally autopicked from 187,076 micrographs and then subjected to one or two rounds of two-dimensional classification to remove obviously bad particles. The remaining 263,477 particles were imported into cryoSPARC for homogenous refinement such that the coordinates of the cargoes in NPC could be determined. Using the new coordinates of the cargoes, 193,636 particles were extracted with a box size of 640 pixels (binned 1×, 0.668 Å per pixel). These particles were then subjected to one or two rounds of two-dimensional classification to remove obviously bad particles, retaining 180,460 for 3D classification with a 60 Å low-pass-filtered reference map (EMD-0220) in RELION3.1 (ref. 56). The best 3D classes (97,909 particles) were selected for initial 3D homogenous refinement with CTF in cryoSPARC 3.2. Next, these 97,909 particles were subjected to heterogeneous refinement in cryoSPARC with three models (the best class from the above 3D classification in RELION, EMD-8346 and a ball-like reference). The class with best quality was further subjected to non-uniform refinement[57], which resulted in a 2.79 Å map with 86,343 particles. After a round of CTF refinement and non-uniform refinement, resolution was finally improved to 2.64 Å. To improve the local density quality of export factors, different masks were applied separately to the regions of three Mex67–Mtr2 heterodimers and Gle2, and their coordinates were recentred to re-extract particles for further refinement in these regions. Briefly, local refinement with soft masks was performed to further optimize pose parameters. The particles were then recentred and extracted using the refined pose parameters. Finally, the extracted particles were subjected to non-uniform refinement using cryoSPARC 3.2, after which resolution had improved to 3.81, 5.80, 5.88 and 10 Å for the three Mex67–Mtr2 heterodimers and Gle2, respectively. For Crm1, only local refinement with a soft mask was performed to improve its density quality, with a final resolution of 9.61 Å.

Interactions between pre-60S ribosome and FG repeats

Previous studies have shown that certain export factors interact with FG repeats from FG-containing nucleoporins. In the low-resolution pre-60S map we found some extra densities around the intersubunit surface shown in Extended Data Fig. 8a, implying potential interactions between these export factors and FG repeats. To further confirm this, pre-60S particles were recentred to each export factor and then recentred with a box size of 256 pixels. The re-extracted particles were used for 3D reconstruction without alignment. From these maps, extra densities were indeed found surrounding the export factors. For convenience of analysis we combined the maps of these export factors and the pre-60S particle using a normalized module of EMAN2 (e2proc3d.py–process = normalize.local)[58], which enables synchronous representation of densities at a comparable threshold.

Distribution of NPC-trapped pre-60S particles and bound Mex67–Mtr2 heterodimers in the NPC channel

To measure the relative position of pre-60S particles in the NPC we reconstructed the structures of pre-60S and NPC respectively and projected each particle of pre-60S on the NPC using the derived coordinates and Euler angle parameters (Extended Data Fig. 10). Distances from the centre of pre-60S to the symmetry axis and the equatorial plane of NPC were calculated as follows: (1) we determined the NPC symmetry axis for each NPC particle based on Euler angles obtained during reconstruction. (2) We then estimated the distance (d_1) between the alignment centre of pre-60S (approximately equal to the centre of mass) and that of the NPC using the coordinates of both. (3) We calculated the angle (θ) between d_1 and the equatorial plane of the NPC using the NPC symmetry axis and pre-60S vectors; d_2 is defined as the projection of d_1 on the symmetry axis of the NPC—that is, the height of the pre-60S particle along the NPC symmetry axis; d_3 is defined as the distance from the centre of pre-60S to the symmetry axis of the NPC. When imaging by transmission electron microscopy, the information along the *z* direction is missing (for top- and side-view, NPCs are d_2 and d_3 here, respectively). Therefore, distance d_3 is equal to $d_1 \times \cos\theta$ for top-view NPCs and height d_2 is equal to $d_1 \times \sin\theta$ for side-view NPCs.

The remapping methodology is now described.

(1) Projection of pre-60S. As mentioned above, 86,343 particles were used for reconstruction of pre-60S (pre-60S.mrc), yielding a star file (pre-60S.star) including coordinates and Euler angles of pre-60S. Using the command (relion_project --i pre-60S.mrc --ang pre-60S.star --o pre-60S_projection) in RELION, we projected pre-60S particles back to raw images (pre-60S_projection.mrcs).
(2) Reconstruction and projection of NPC. Using the coordinates of pre-60S, we extracted 86,343 NPC particles in a large box size of 2,480 pixels. After 3D reconstruction we obtained a cryo-EM map and a star file including coordinates and Euler angles of the NPC. Similar to step 1, we projected NPC particles back to raw images (NPC_projection.mrcs).
(3) Superposition of projections. Using the command (relion_image_handler --i pre-60S.mrcs --add NPC.mrcs --o superposition) in RELION, we acquire the orientational relationship of each pre-60S and corresponding NPC.

Numpy[59] and matplotlib[60] were used to plot statistical graphics. Using a similar method, remapping and distribution of the three Mex67–Mtr2 heterodimers was performed. Representative projection superpositions are shown in Extended Data Fig. 9.

Structural prediction of the Gle2–Rlp24 complex by AlphaFold-Multimer

The structure of the Gle2–Rlp24 complex in this study was generated from AlphaFold-Multimer[61] with the full-length protein sequences of Gle2 and Rlp24 from *S. cerevisiae* as input. Followed by default setting within multimer mode, five AlphaFold-Multimer initial models were produced, each model runed five iterations to output a total of 25 predicted models. Based on template modelling scores and predicted alignment error values for each model, we then picked the top-ranked structure of the protein–protein complex with the most confident score as the final model for subsequent analysis. The structures of Gle2 and the C-terminal of Rlp24 from *Homo sapiens* and *Mus musculus* were predicted using a similar method.

Model building and refinement

The atomic coordinate of the yeast early cytoplasmic-immediate pre-60S ribosome (PDB 6N8K) was used as the initial template for building the bulk of NPC-trapped particles. Models of rRNAs (25S, 5.8S and 5S), r-proteins (uL1-eL43) and assembly factors (Mrt4, Bud20, Alb1, Nog1, Rlp24, NMD3, Nog2, Nsa2, Tif6 and YBL028C) were docked into the density map manually using UCSF Chimera[62] and adjusted with COOT[63], based on density and sequences. The ES27 and Arx1 models were extracted from the Rix-Rea1 pre-60S particle (PDB 5FL8)[33] and fitted into its density by rigid-body docking followed by a similar manual adjustment in COOT. In our model, these rRNAs (except for H69–H71) and r-proteins include almost complete sequence information. The crystal structure of yeast Mex67–Mtr2 (PDB 4WWU)[64] was docked into the density map. For modelling of Ecm1, all known assembly factors were screened individually and the predicted structure of Ecm1 by AlphaFold 2 was selected as the initial target. Residues of 107–159 showed a perfect fit with density. For Crm1 and Gle2, the crystal structure of Crm1–RanGTP (3NC1)[65] and the AlphaFold 2-predicted structure were separately fit to their density by rigid-body docking. Real-space refinement and final validation of the NPC-trapped particle model were performed using the real-space refine and validation programme from PHENIX[66]. Structural visualizations and figures were performed with UCSF Chimera, Chimera X[67] and PyMOL (www.pymol.org).

Reporting summary

Further information on research design is available in the Nature Portfolio Reporting Summary linked to this article.

Data availability

The electron microscopy density map of the NPC-trapped pre-60S particle (EMD-34725), local refinement maps of export factors—including Mex67–Mtr2-1 (EMD-34638), Mex67–Mtr2-2 (EMD-34640), Mex67–Mtr2-3 (EMD-35767) and Crm1 (EMD-34641)—and Bud20 (EMD-35812) have been deposited in the Electron Microscopy Data Bank (http://www.ebi.ac.uk/pdbe/emdb/). Atomic coordinates of the NPC-trapped pre-60S particle (PDB 8HFR) and Mex67–Mtr2-1 (PDB 8HBN) have been deposited in the Protein Data Bank (http://www.rcsb.org).

51. Mastronarde, D. N. Automated electron microscope tomography using robust prediction of specimen movements. *J. Struct. Biol.* **152**, 36–51 (2005).
52. Zheng, S. Q. et al. MotionCor2: anisotropic correction of beam-induced motion for improved cryo-electron microscopy. *Nat. Methods* **14**, 331–332 (2017).
53. Punjani, A., Rubinstein, J. L., Fleet, D. J. & Brubaker, M. A. cryoSPARC: algorithms for rapid unsupervised cryo-EM structure determination. *Nat. Methods* **14**, 290–296 (2017).
54. Zhang, K. Gctf: real-time CTF determination and correction. *J. Struct. Biol.* **193**, 1–12 (2016).
55. Rohou, A. & Grigorieff, N. CTFFIND4: fast and accurate defocus estimation from electron micrographs. *J. Struct. Biol.* **192**, 216–221 (2015).
56. Scheres, S. H. RELION: implementation of a Bayesian approach to cryo-EM structure determination. *J. Struct. Biol.* **180**, 519–530 (2012).
57. Punjani, A., Zhang, H. & Fleet, D. J. Non-uniform refinement: adaptive regularization improves single-particle cryo-EM reconstruction. *Nat. Methods* **17**, 1214–1221 (2020).
58. Tang, G. et al. EMAN2: an extensible image processing suite for electron microscopy. *J. Struct. Biol.* **157**, 38–46 (2007).
59. Harris, C. R. et al. Array programming with NumPy. *Nature* **585**, 357–362 (2020).
60. Hunter, J. D. Matplotlib: a 2D graphics environment. *Comput. Sci. Eng.* **9**, 90–95 (2007).
61. Evans, R. et al. Protein complex prediction with AlphaFold-Multimer. Preprint at *bioRxiv* https://doi.org/10.1101/2021.10.04.463034 (2022).
62. Pettersen, E. F. et al. UCSF Chimera—a visualization system for exploratory research and analysis. *J. Comput. Chem.* **25**, 1605–1612 (2004).
63. Emsley, P. & Cowtan, K. Coot: model-building tools for molecular graphics. *Acta Crystallogr. D Biol. Crystallogr.* **60**, 2126–2132 (2004).
64. Aibara, S., Valkov, E., Lamers, M. & Stewart, M. Domain organization within the nuclear export factor Mex67:Mtr2 generates an extended mRNA binding surface. *Nucleic Acids Res.* **43**, 1927–1936 (2015).
65. Guttler, T. et al. NES consensus redefined by structures of PKI-type and Rev-type nuclear export signals bound to CRM1. *Nat. Struct. Mol. Biol.* **17**, 1367–1376 (2010).
66. Adams, P. D. et al. PHENIX: a comprehensive Python-based system for macromolecular structure solution. *Acta Crystallogr. D Biol. Crystallogr.* **66**, 213–221 (2010).
67. Pettersen, E. F. et al. UCSF ChimeraX: structure visualization for researchers, educators, and developers. *Protein Sci.* **30**, 70–82 (2021).

Acknowledgements We thank the staff at both the cryo-EM centre of South University of Science and Technology and the Tsinghua University Branch of the National Protein Science Facility (Beijing) for their technical support on the cryo-EM and high-performance computation platforms. We thank Y. Zhang and Y. Li for helpful discussions. This work was supported by the National Natural Science Foundation of China (nos. 32071192/32271245 to S.-F.S. and 32230051 to N.G.) and by Tsinghua-Peking Center for Life Sciences (to L.Z. and Z.L.).

Author contributions S.-F.S. supervised the project. Z.L. established the yeast strain and prepared samples for electron microscopy. L.Z., S.C., Z.L. and H.X. collected electron microscopy data. S.C. solved the structure of the pre-60S particle. S.C., L.Z. and G.H. performed electron microscopy analysis. S.C. and X.Y. analysed pre-60S particle distribution in the NPC channel. Z.L. and S.C. performed model building and structure refinement. S.C. performed AlphaFold-Multimer model generation. P.W. participated in electron microscopy data collection. Z.L., S.C., N.G. and S.-F.S. analysed the structure. Z.L. and S.C. jointly wrote the initial draft. N.G. and S.-F.S. edited the manuscript.

Competing interests The authors declare no competing interests.

Additional information

Supplementary information The online version contains supplementary material available at https://doi.org/10.1038/s41586-023-06128-y.

Correspondence and requests for materials should be addressed to Sen-Fang Sui.

Peer review information *Nature* thanks Vikram Panse and the other, anonymous, reviewer(s) for their contribution to the peer review of this work.

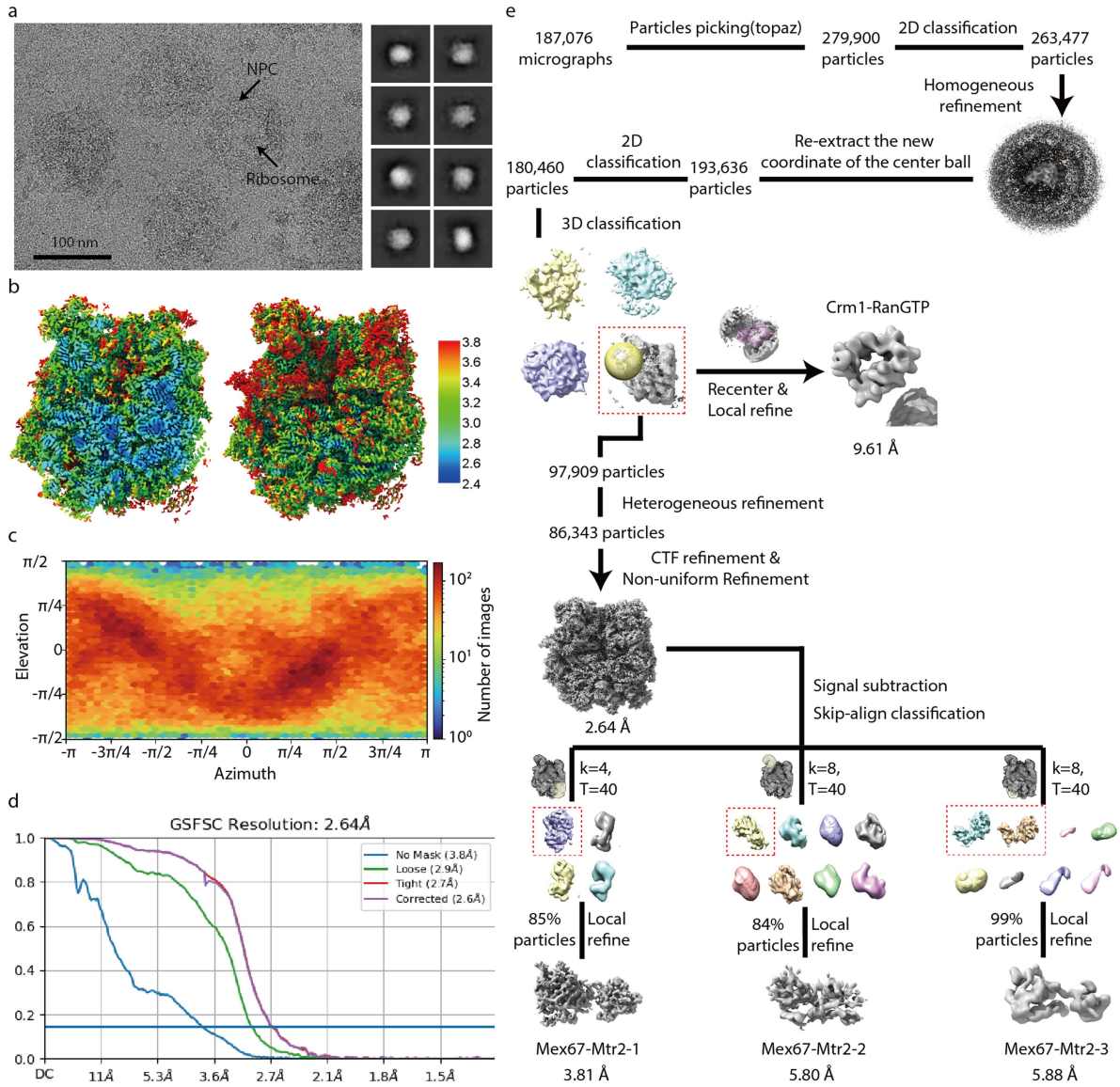

Extended Data Fig. 1 | Cryo-EM data analysis of the NPC-trapped pre-60S ribosome. a, A representative raw micrograph of the pre-60S containing NPC particles from similar 187,076 micrographs and representative 2D class averages of pre-60S are shown on the right from selected 279,900 particles. **b**, Local resolution map for a central slice (left) and the overall 3D reconstruction (right). **c**, Angular distribution of particles used for the 3D reconstruction. **d**, FSC curves for the cryo-EM map of NPC-trapped pre-60S particle. The threshold of 0.143 was used to determine the overall resolution of the map. **e**, Flowcharts for cryo-EM data processing. See "Methods" for details.

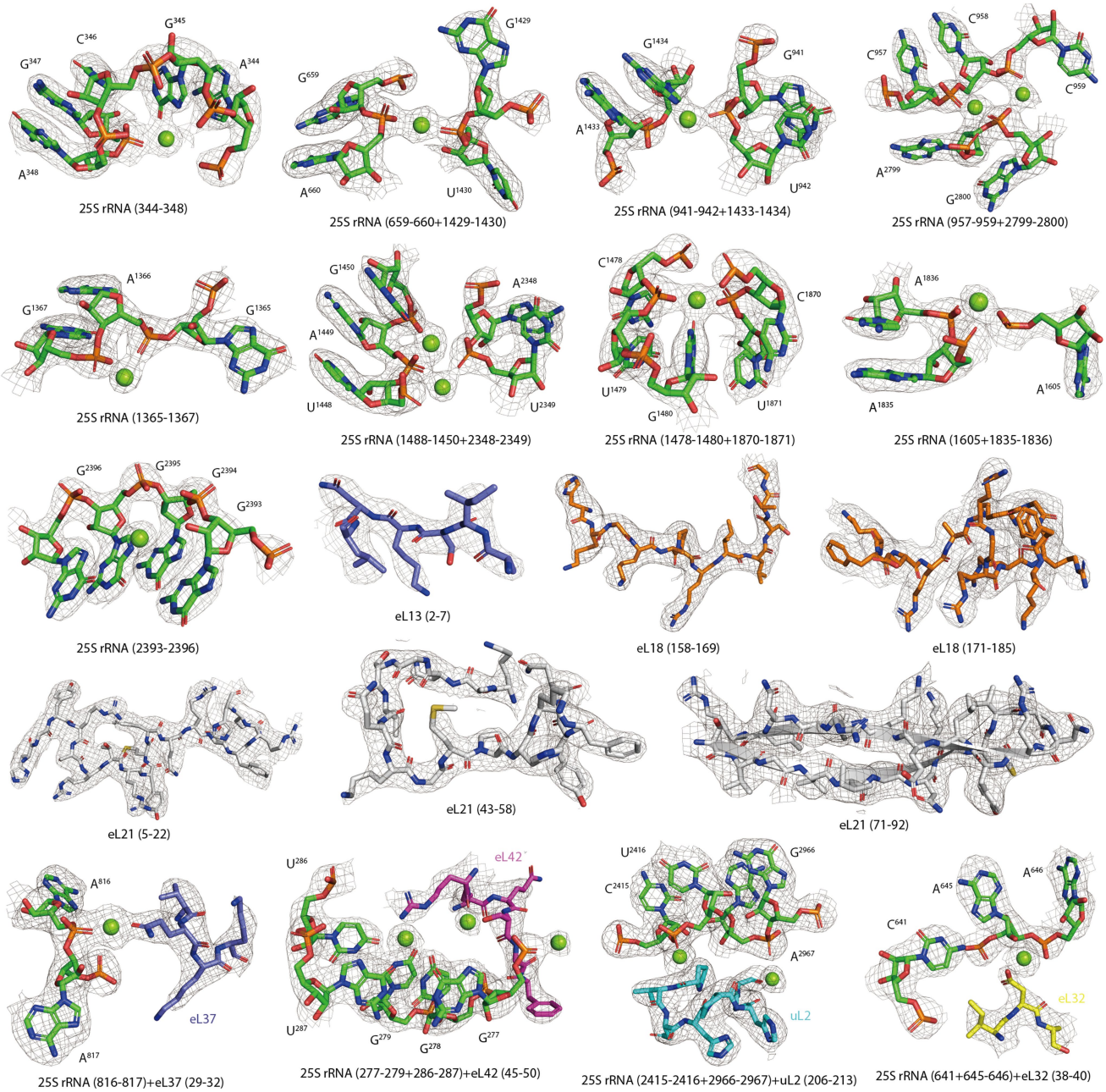

Extended Data Fig. 2 | Density presentation of the NPC-trapped pre-60S particle. Representative density maps of proteins and rRNAs from the NPC-trapped pre-60S particle. Different fashions of interactions between magnesium ions and pre-60S particle, and newly identified regions from ribosomal proteins are shown. Magnesium ions are displayed as spheres.

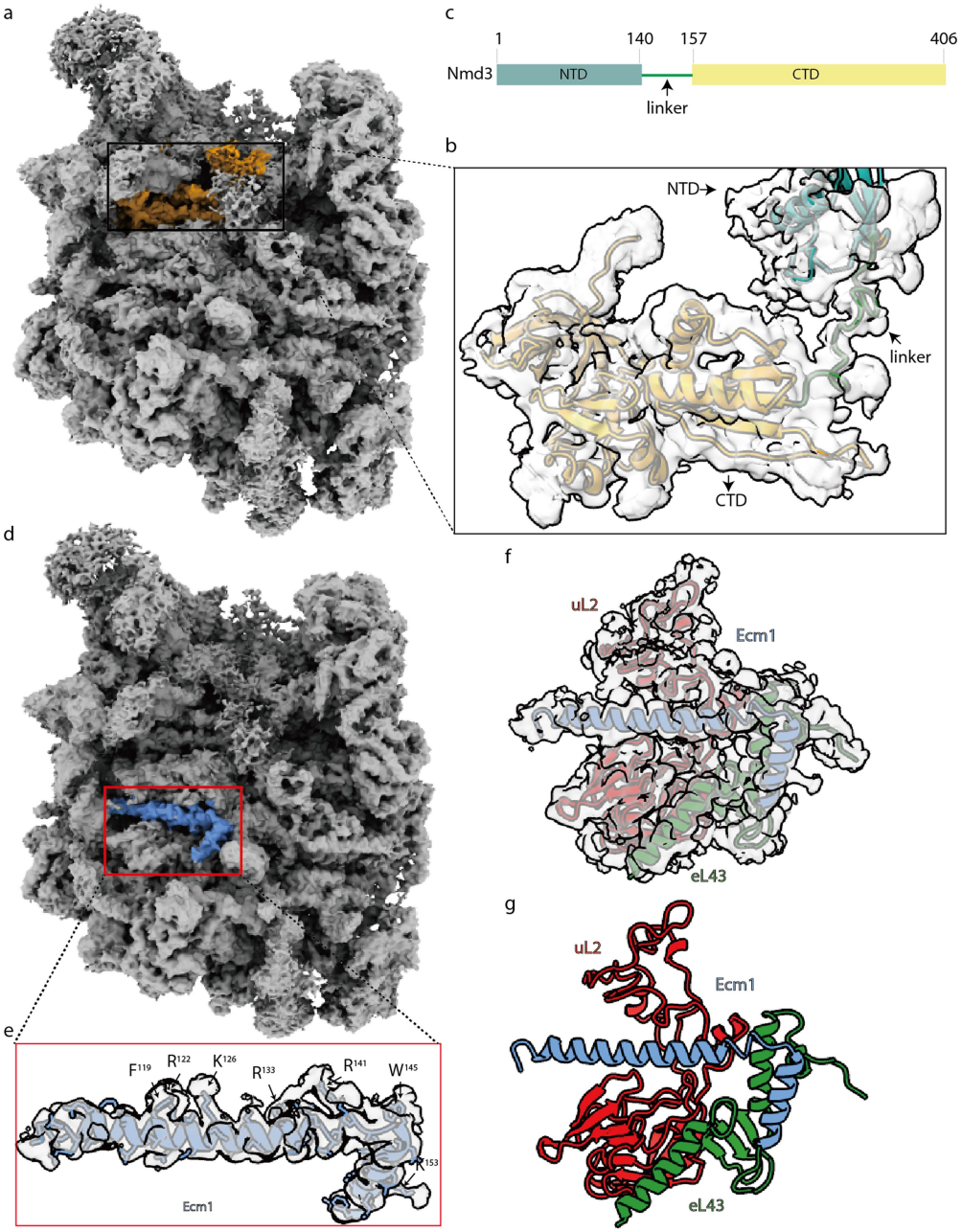

Extended Data Fig. 3 | Identifications of Nmd3-NTD and Ecm1. a, The position of Nmd3 in the NPC-trapped pre-60S particle is colored as orange, boxed by black frame and enlarged in (**b**). **b**, Fitting of Nmd3 into the map. The density is displayed as transparent surface representation. The NTD, CTD and the linker between NTD and CTD are color coded. **c**, Schematic representation of the domain structures of Nmd3. Domains are color coded as in (**b**). **d**, The extra density of two helices is located between L1 stalk and H34, boxed by red frame and enlarged in (**e**). **e**, Fitting of Ecm1 (aa 107 to 159) into the map. The density is displayed as transparent surface representation and bulky side chains of several residues are shown as models. **f**-**g**, Interactions between Ecm1 and uL2 and eL43 are shown as transparent surface representation (**f**) and cartoon (**g**). These results are consistent with the previous mass spectrometry identification[49].

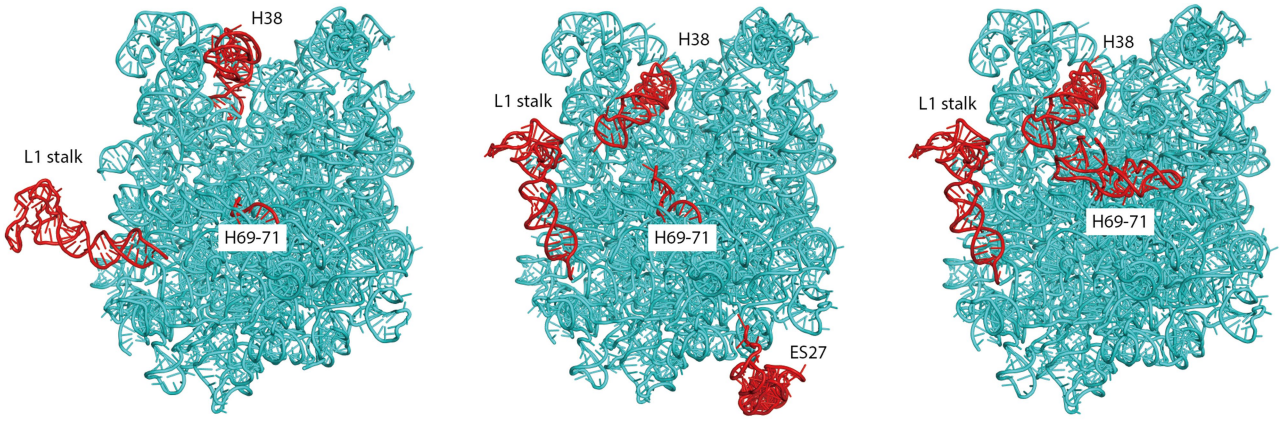

Extended Data Fig. 4 | Changed regions of the 25S rRNA upon nuclear export of pre-60S particle. Compared with the structures of pre-60S particles before nuclear export (left) and after nuclear export (right), four regions of rRNA (red) suffer dramatic conformational change including H38, L1 stalk, H69-71 and ES27. The unchanged bulk of rRNA is colored cyan.

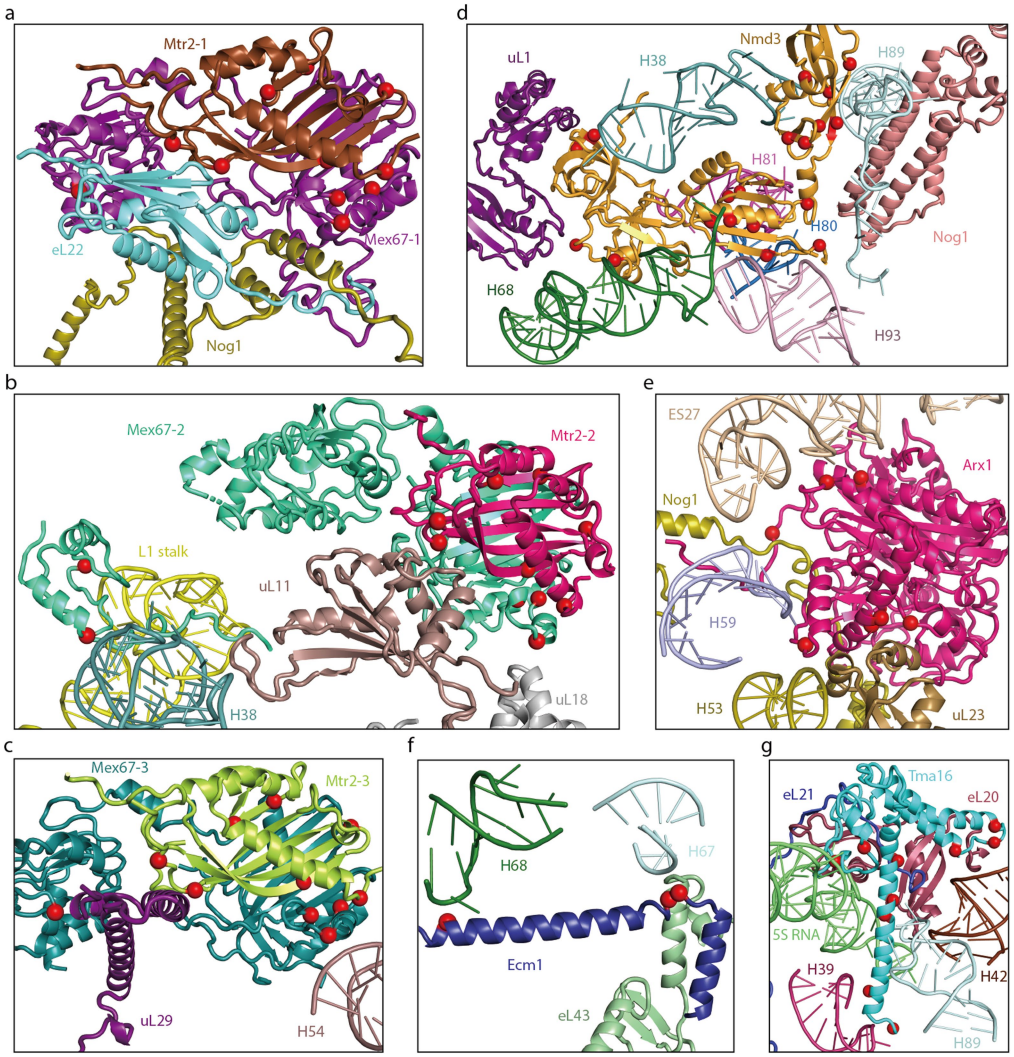

Extended Data Fig. 5 | Export factors and disease-related mutations. **a**–**g**, Conserved cancer related mutations of the human export factors are mapped in the interfaces between pre-60S particle and Mex67-Mtr2-1 (**a**), Mex67-Mtr2-2 (**b**), Mex67-Mtr2-3 (**c**), Nmd3 (**d**), Arx1 (**e**), Ecm1 (**f**) and Tma16 (**g**). Mutation positions are shown as spheres.

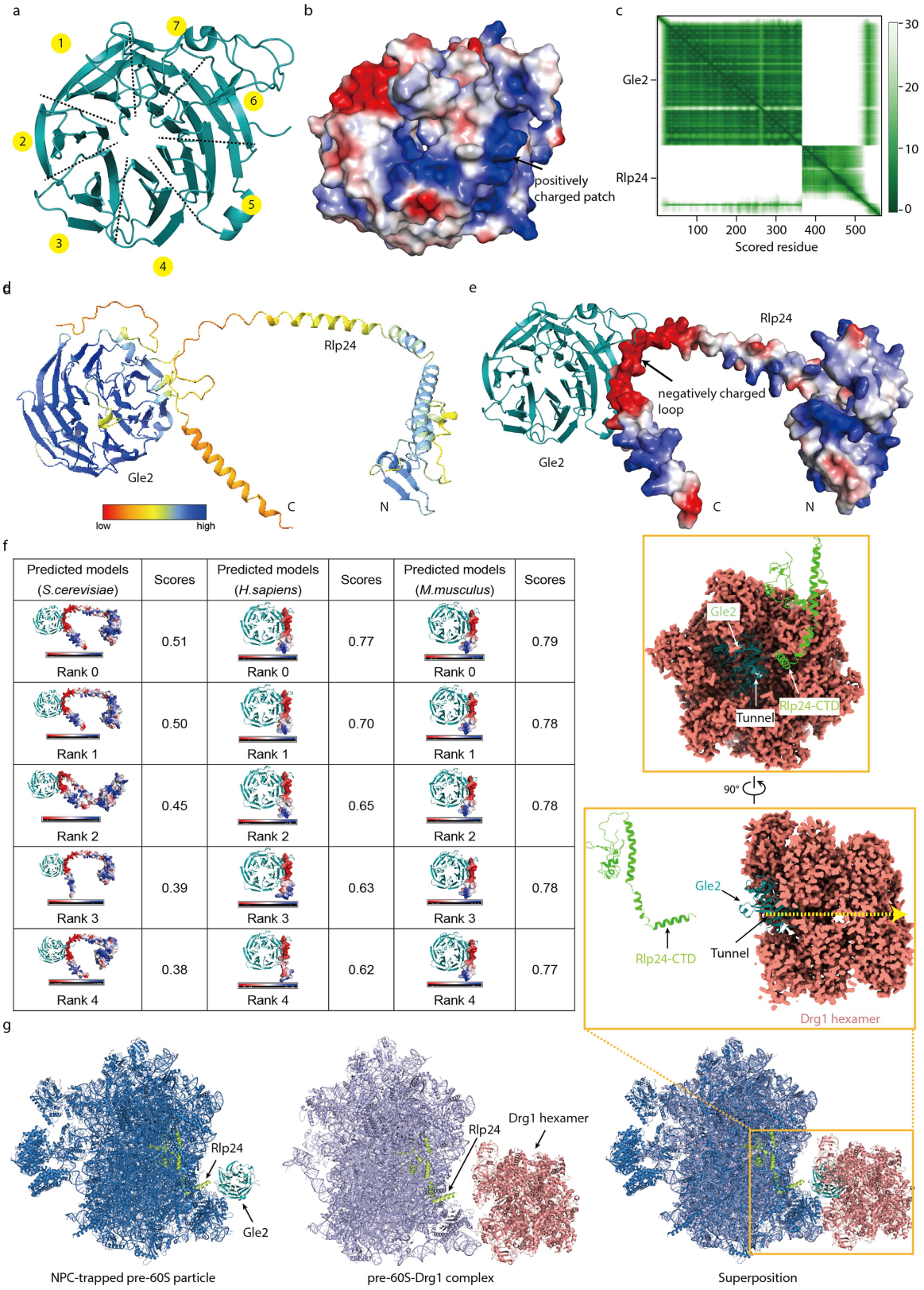

Predicted models (*S.cerevisiae*)	Scores	Predicted models (*H.sapiens*)	Scores	Predicted models (*M.musculus*)	Scores
Rank 0	0.51	Rank 0	0.77	Rank 0	0.79
Rank 1	0.50	Rank 1	0.70	Rank 1	0.78
Rank 2	0.45	Rank 2	0.65	Rank 2	0.78
Rank 3	0.39	Rank 3	0.63	Rank 3	0.78
Rank 4	0.38	Rank 4	0.62	Rank 4	0.77

Extended Data Fig. 6 | See next page for caption.

Extended Data Fig. 6 | Interaction between Gle2 and Rlp24 predicted by AlphaFold-Multimer. a, The structure of Gle2 contains seven WD40 domains. **b**, Surface electrostatic potentials of Gle2 displays a positively charged patch. **c**-**d**, The predicted Gle2-Rlp24 structure (**d**) and the associated PAE (predicted alignment error) value (**c**). Confidence level of PAE: Dark green is good (low error), light green is bad (high error). **e**, The predicted Gle2-Rlp24 structure shows that the negatively charged loop of Rlp24 is embedded into the positively charged patch of Gle2. **f**, Representative top5 models of the predicted Gle2-Rlp24 structures from *S.cerevisiae* (left column) and the top5 models of the predicted Gle2 and C-terminal of Rlp24 from *H.sapiens* (middle column) and *M.musculus* (right column), suggesting that a conserved negatively charged motif in the C-terminal of Rlp24 is responsible for binding to Gle2. **g**, Structural comparison of NPC-trapped pre-60S particle (left panel: skyblue, Rlp24: limon, Gle2: teal) and pre-60S-Drg1 complex (middle panel: lightblue, Drg1 hexamer: salmon). The positional relationship of Rlp24, Gle2 and Drg1 hexamer is enlarged in top view (left) and side view (right, central slice) at the bottom.

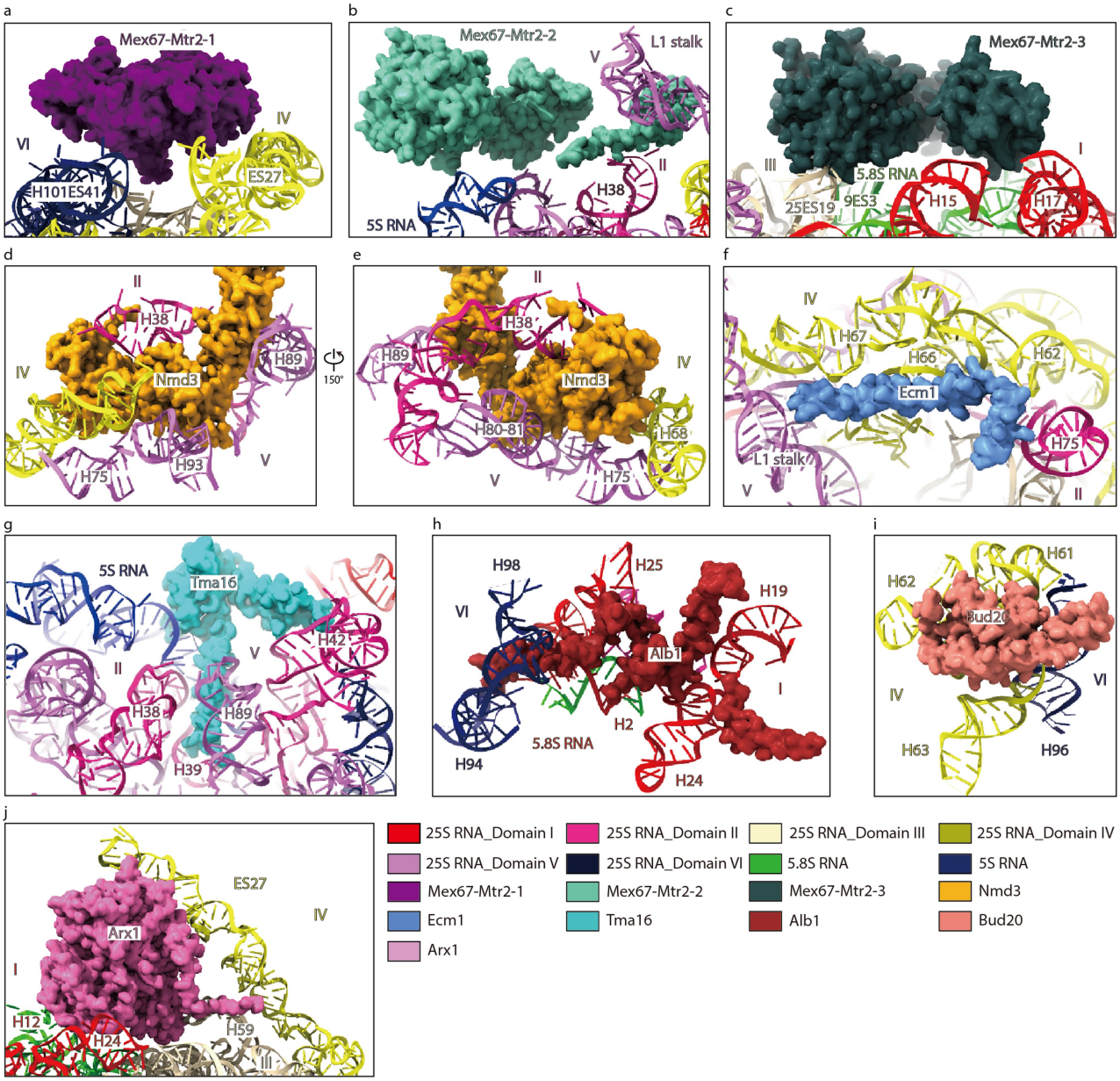

Extended Data Fig. 7 | Export factors bind to the flexible or protruding regions of rRNA and connect different domains of rRNAs. a, Mex67-Mtr2-1 connects the domain IV and domain VI through interactions with ES27 and H101ES41. **b**, Mex67-Mtr2-2 simultaneously interacts with 5S RNA, H38 from domain II and the L1 stalk from domain V. **c**, The domain I, domain III and the 5.8S RNA are bridged by Mex67-Mtr2-3. **d**-**e**, Nmd3 is enclosed by domain II, domain IV and domain V through extensive interactions with H38, H68, H75, H80-81, H89 and H93. **f**, Ecm1 connects scaffolds domain II, domain IV and domain V by binding to H75, H62, H66, H67 and L1 stalk. **g**, Tma16 bridges the domain II, domain V and 5S RNA to prevent the pre-maturation of the CP and P0 stalk. **h**, Alb1 links the 5.8S RNA, domain I and domain VI through interactions with H2, H19, H24, H25, H94 and H98. **i**, Bud20 is clamped between the H61-H63 from domain IV and H96 from domain VI. **j**, Arx1 is sandwiched by the flexible ES27 from domain IV, H12 and H24 from domain I and H59 from domain III. Export factors and rRNAs are shown in surface and cartoon representation, respectively. Different export factors and rRNA domains are color coded.

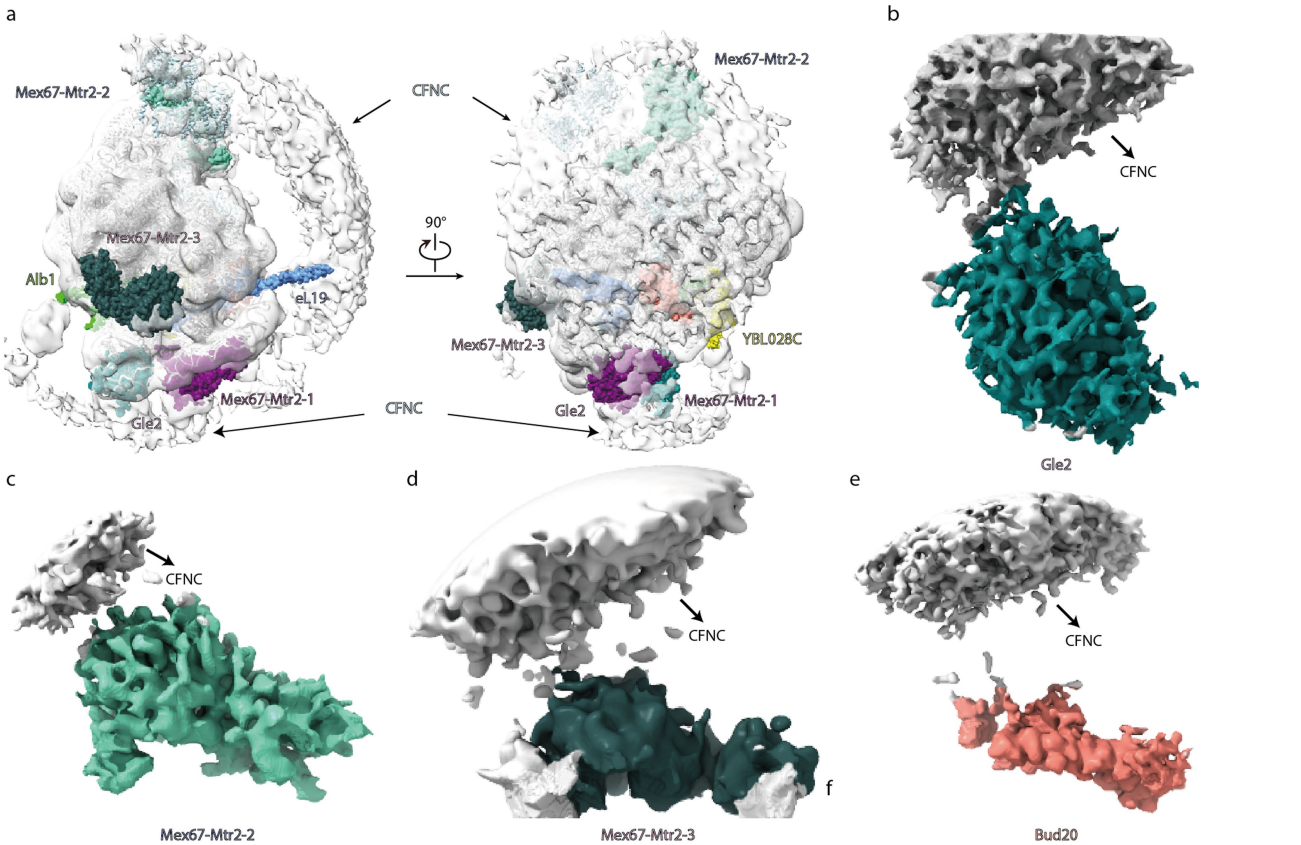

Extended Data Fig. 8 | Export factors interact with NPC. a, The map of NPC-trapped pre-60S particle displayed in a low threshold, highlighting numerous extra densities connected to export factors. These densities could be assigned to the central FG Nups and/or NTFs with/without cargoes (CFNC) including FG-repeats omitted from the wall of NPC. The eL19 and YBL028C obviously interact with the extra density, suggesting a possible role in direct interactions with the NPC. **b**–**e**, Local refinements of Gle2 (**b**), Mex67-Mtr2-2 (**c**), Mex67-Mtr2-3 (**d**) and Bud20 (**e**) further show the interactions between these export factors and the NPC.

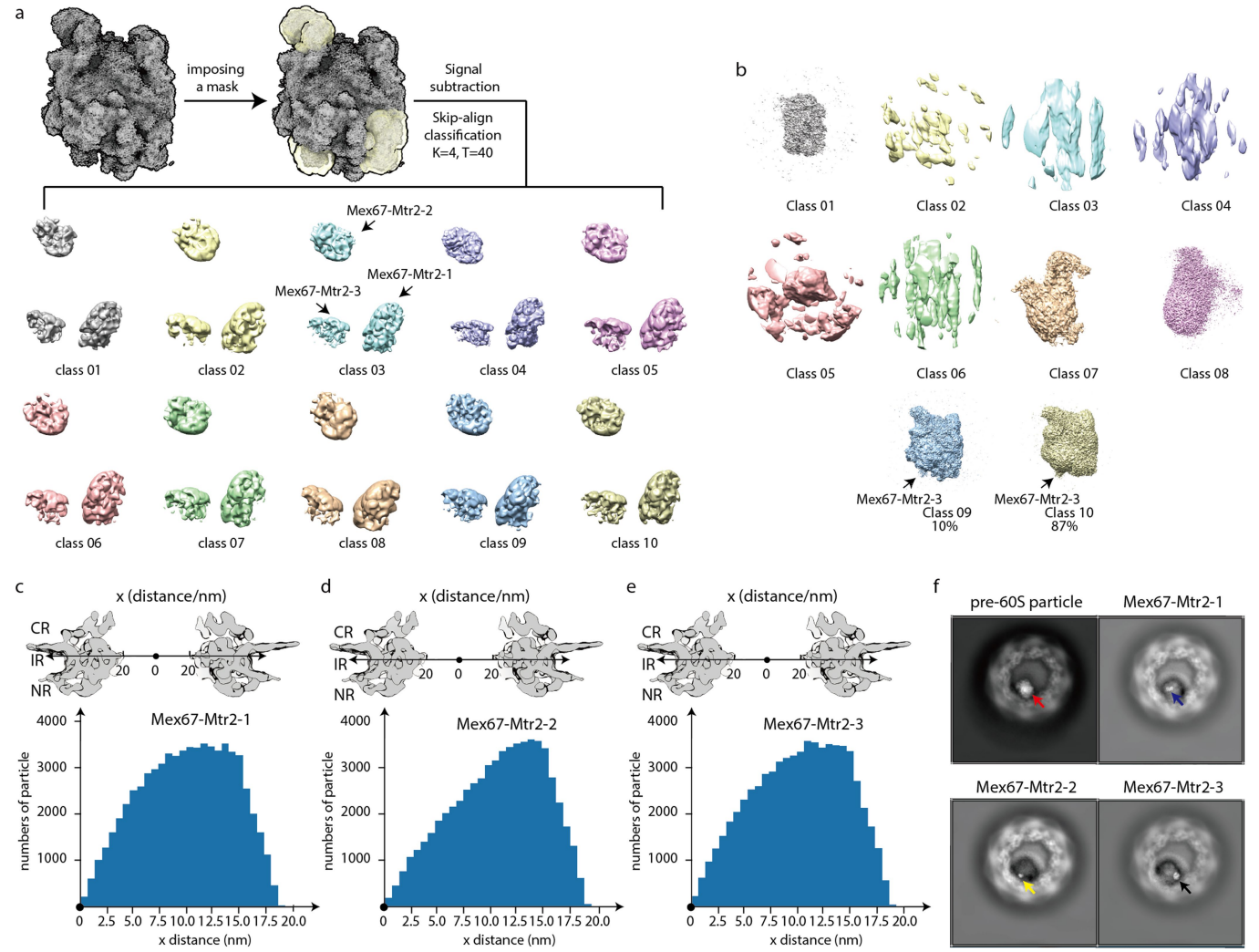

Extended Data Fig. 9 | Heterogeneity analysis, distribution and remapping of representative pre-60S particles and three bound Mex67-Mtr2 respectively. a-b, Skip-align classifications of the three Mex67-Mtr2 modules (**a**) and the entire pre-60S particles (**b**). **c**–**e**, The radial distribution of Mex67-Mtr2-1 (**c**), Mex67-Mtr2-2 (**d**) and Mex67-Mtr2-3 (**e**) within the NPC. **f**, The pre-60S particles and three Mex67-Mtr2 are remapped back into the same NPC showing in top-view. The relative position of the pre-60S particles (red arrow), Mex67-Mtr2-1 (blue arrow), Mex67-Mtr2-2 (yellow arrow) and Mex67-Mtr2-3 (black arrow) are indicated.

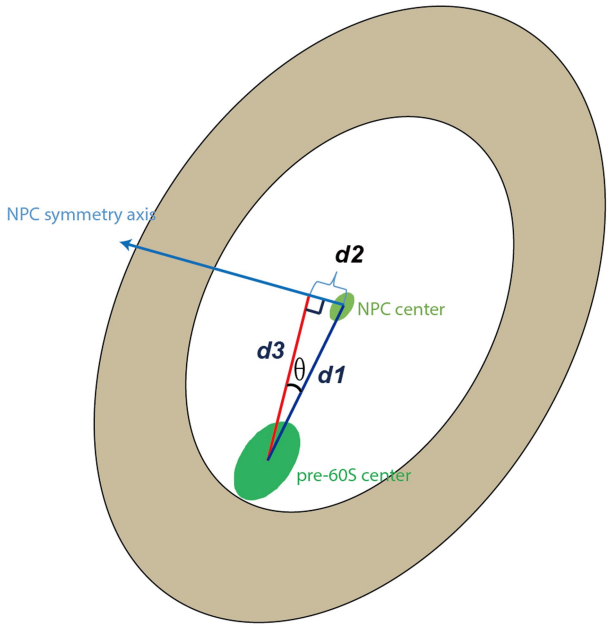

Extended Data Fig. 10 | Measurement diagram of the relative position of pre-60S particles in the NPC. *d1* represents the projection distance between the center of NPC and the center of pre-60S in the micrograph, *d2* is the projection of *d1* on the symmetry axis of NPC, that is, the distance from the center of pre-60S to the equatorial plane of NPC, and *d3* is the distance from the center of pre-60S to the symmetry axis of NPC.

Extended Data Table 1 | Cryo-EM data collection, refinement and validation statistics

	NPC-trapped pre-60S (EMD-34725) (PDB 8HFR)	Mex67-Mtr2-1 (EMD-34638) (PDB 8HBN)	Mex67-Mtr2-2 (EMD-34640)	Mex67-Mtr2-3 (EMD-35767)	Crm1 (EMD-34641)	Bud20 (EMD-35812)
Data collection and processing						
Magnification	130,000	130,000	130,000	130,000	130,000	130,000
Voltage (kV)	300	300	300	300	300	300
Camera	K3	K3	K3	K3	K3	K3
Electron exposure (e^{-}/Å^2)	50	50	50	50	50	50
Defocus range (μm)	-1.5 ~ -2.5	-1.5 ~ -2.5	-1.5 ~ -2.5	-1.5 ~ -2.5	-1.5 ~ -2.5	-1.5 ~ -2.5
Pixel size (Å)	0.668	0.668	0.668	0.668	0.668	0.668
Initial particle images (no.)	279,900	86,343	86,343	86,343	279,900	86,343
Final particle images (no.)	86,343	73,392	72,528	86,480	97,909	86,343
Symmetry imposed	C1	C1	C1	C1	C1	C1
Map resolution (Å)	2.64	3.81	5.80	5.88	9.61	3.11
Map sharpen B factor (Å^2)	-51.9	-99.5	-522.8	-550.0	-1000.0	-111.6
FSC threshold	0.143	0.143	0.143	0.143	0.143	0.143
Map resolution range (Å)	2.4-3.8	3.0-5.6	5.6-6.2	5.8-6.9	9.5-11.0	3.2-3.9
Refinement						
Initial model used	6N8K, 5FL8, 4WWU	4WWU				
Model resolution (Å)	2.64	3.81				
FSC threshold	0.143	0.143				
Model resolution range (Å)	2.4-3.8	3.0-5.6				
Model composition						
Non-hydrogen atoms	152481	4189				
Protein residues	10776	536				
Nucleotides	3551	0				
Ligands	237	0				
B factors (Å2)						
Protein	14.78	33.70				
Nucleotide	15.95					
Ligand	30.00					
R.m.s. deviations						
Bond lengths (Å)	0.007	0.007				
Bond angles (°)	1.064	1.392				
Validation						
MolProbity score	1.48	2.79				
Clashscore	2.31	13.75				
Rotamer outliers (%)	0.60	6.10				
Ramachandran plot						
Favored (%)	92.30	89.96				
Allowed (%)	7.51	7.39				
Disallowed (%)	0.19	2.65				

nature portfolio

Corresponding author(s): Sen-Fang Sui

Last updated by author(s): Apr 8, 2023

Reporting Summary

Nature Portfolio wishes to improve the reproducibility of the work that we publish. This form provides structure for consistency and transparency in reporting. For further information on Nature Portfolio policies, see our Editorial Policies and the Editorial Policy Checklist.

Statistics

For all statistical analyses, confirm that the following items are present in the figure legend, table legend, main text, or Methods section.

n/a	Confirmed
☐	☒ The exact sample size (*n*) for each experimental group/condition, given as a discrete number and unit of measurement
☐	☒ A statement on whether measurements were taken from distinct samples or whether the same sample was measured repeatedly
☒	☐ The statistical test(s) used AND whether they are one- or two-sided *Only common tests should be described solely by name; describe more complex techniques in the Methods section.*
☒	☐ A description of all covariates tested
☒	☐ A description of any assumptions or corrections, such as tests of normality and adjustment for multiple comparisons
☒	☐ A full description of the statistical parameters including central tendency (e.g. means) or other basic estimates (e.g. regression coefficient) AND variation (e.g. standard deviation) or associated estimates of uncertainty (e.g. confidence intervals)
☒	☐ For null hypothesis testing, the test statistic (e.g. *F*, *t*, *r*) with confidence intervals, effect sizes, degrees of freedom and *P* value noted *Give P values as exact values whenever suitable.*
☒	☐ For Bayesian analysis, information on the choice of priors and Markov chain Monte Carlo settings
☒	☐ For hierarchical and complex designs, identification of the appropriate level for tests and full reporting of outcomes
☒	☐ Estimates of effect sizes (e.g. Cohen's *d*, Pearson's *r*), indicating how they were calculated

Our web collection on statistics for biologists contains articles on many of the points above.

Software and code

Policy information about availability of computer code

Data collection	serialEM 3.7.13
Data analysis	MotionCor2 1.1.0, cryoSPARC 3.2 Gctf CTFFIND4.1, RELION 3.1, RELION 4.0, EMAN2.91, Phenix 1.14-3260, Coot 0.8.9.1, Numpy 1.17.4, matplotlib 3.6.0, Pymol 1.8.2.1, Chimera 1.16, ChimeraX 1.4, AlphaFold 2.0,

For manuscripts utilizing custom algorithms or software that are central to the research but not yet described in published literature, software must be made available to editors and reviewers. We strongly encourage code deposition in a community repository (e.g. GitHub). See the Nature Portfolio guidelines for submitting code & software for further information.

Data

Policy information about availability of data

All manuscripts must include a data availability statement. This statement should provide the following information, where applicable:

- Accession codes, unique identifiers, or web links for publicly available datasets
- A description of any restrictions on data availability
- For clinical datasets or third party data, please ensure that the statement adheres to our policy

The EM density map of the NPC-trapped pre-60S particle (EMD-34725), the local refinement maps of export factors including Mex67-Mtr2-1 (EMD-34638), Mex67-Mtr2-2 (EMD-34640), Mex67-Mtr2-3 (EMD-35767) and Crm1 (EMD-34641), and Bud20 (EMD-35812) have been deposited in the Electron Microscopy Data Bank (http://www.ebi.ac.uk/pdbe/emdb/). Atomic coordinates of the NPC-trapped pre-60S particle (PDB 8HFR) and Mex67-Mtr2-1 (PDB 8HBN) have been deposited in the Protein Data Bank (http://www.rcsb.org).

Field-specific reporting

Please select the one below that is the best fit for your research. If you are not sure, read the appropriate sections before making your selection.

☒ Life sciences ☐ Behavioural & social sciences ☐ Ecological, evolutionary & environmental sciences

For a reference copy of the document with all sections, see nature.com/documents/nr-reporting-summary-flat.pdf

Life sciences study design

All studies must disclose on these points even when the disclosure is negative.

Sample size	Sample size calculation was performed based on the previous knowledge. cryo-EM datasets were collected and generated interpretable map with sufficient resolution reported in this study. Due to the resolution is high (2.64 angstroms), we judged the sample size is enough.
Data exclusions	The exclusion criteria were not pre-established. 2D and 3D classification yielded multiple classes. Only the particles in the classes that showed clear structural signals and intact structures were selected, combined and used in the final reconstruction and refinement. Details are described in the flowchart of Extended Data Figure 1 and Methods.
Replication	The purifications of pre-60S-containing NPC were performed repeatedly at least 10 times and were analyzed by MS with consistent results. The cryo-EM datasets that contains hundreds of thousands of pre-60S particles have inherent replication. The refinements were repeated at least three times with different angle searching range and all resulted in similar density maps (with different resolution though).
Randomization	Gold standard Fourier Shell Correlation method was used to estimate the resolution of the cryo-EM structures, in which the dataset is split into two sets and refined independently. The process of splitting the dataset, odd and even, is considered random.
Blinding	Blinding is not applicable to a cryo-EM experiment, because no human research participants are involved.

Reporting for specific materials, systems and methods

We require information from authors about some types of materials, experimental systems and methods used in many studies. Here, indicate whether each material, system or method listed is relevant to your study. If you are not sure if a list item applies to your research, read the appropriate section before selecting a response.

Materials & experimental systems

n/a	Involved in the study
☒	☐ Antibodies
☒	☐ Eukaryotic cell lines
☒	☐ Palaeontology and archaeology
☒	☐ Animals and other organisms
☒	☐ Human research participants
☒	☐ Clinical data
☒	☐ Dual use research of concern

Methods

n/a	Involved in the study
☒	☐ ChIP-seq
☒	☐ Flow cytometry
☒	☐ MRI-based neuroimaging